Experimental Aero Study on Turbine Rear Structures at Engine-Realistic Flow Conditions

VALENTIN VIKHOREV

Department of Mechanics and Maritime Sciences
CHALMERS UNIVERSITY OF TECHNOLOGY
Gothenburg, Sweden 2021

Thesis for the degree of Licentiate of Engineering

Experimental Aero Study on Turbine Rear Structures at Engine-Realistic Flow Conditions

Valentin Vikhorev

Department of Mechanics and Maritime Sciences
CHALMERS UNIVERSITY OF TECHNOLOGY
Göteborg, Sweden 2021

Experimental Aero Study on Turbine Rear Structures at Engine-Realistic Flow Conditions
Valentin Vikhorev

Thesis for the degree of Licentiate of Engineering
ISSN 2021:19
Department of Mechanics and Maritime Sciences
Chalmers University of Technology
SE–412 96 Göteborg, Sweden
Telephone + 46 (0) 31 – 772 1000

Chalmers Reproservice
Göteborg, Sweden 2021

Abstract

Experimental Aero Study on Turbine Rear Structures at Engine-Realistic Flow Conditions
Thesis for the degree of Licentiate of Engineering in Thermo and Fluid Dynamics
VALENTIN VIKHOREV
Department of Mechanics and Maritime Sciences
Division of Fluid Dynamics
Chalmers University of Technology

The aviation industry has made great progress in continuous improvements that reduce the key pollutants associated with aero engines. However, high demands on the aviation industry drive manufacturers and designers to develop even more efficient aero engines. The introduction of a geared turbofan engine (GTF) was a breakthrough, although it created new challenges for suppliers and designers of individual components. The subject of this thesis is a study of the novel turbine rear structure (TRS) and the effects of its geometric features, such as the polygonal shape of the shroud endwall, thickening of the outlet guide vanes (OGV), and implementation of bumps, with an overall analysis of TRS aerodynamics in terms of possible flow separations, corresponding pressure losses, and flow turning performance.

This work summarizes the results obtained from experimental studies of the engine-realistic TRS for two design configurations: baseline (annular) and state-of-the-art (polygonal) designs equipped with OGVs of different geometries. Each of these two concepts was assembled and aerodynamically investigated for the on-design and off-design conditions in a modern 1.5 stage facility (Chalmers OGV-LPT rig) which provides realistic boundary conditions for the TRS. The aerodynamic study was performed by traverse pressure measurements for the inlet and outlet planes by multi-hole pressure probes, oil-film visualization, and static pressure measurements with embedded pressure taps. Steady state RANS simulations of the TRS were also done to estimate the prediction capabilities of a commercial CFD tool.

OGVs with increased thickness introduce slight increase of pressure losses, although the bump vane with add-on does influence the flow substantially. Apart from downstream influence with additional vorticity, generated from bump itself, and corresponding increased pressure losses, it also has upstream influence indirectly affecting inlet conditions into the TRS. For baseline configuration, the higher inlet swirl angles in the hub region result in increased vane loading and pressure losses. For state-of-the art configuration, blade- and bump-loading analysis show clear mutual influence of the bump and vane pressure distributions and, therefore, the need to design the vane and bump combination as one aerodynamic unit. Moreover, the present work gives a thorough comparison between experimental and numerical data showing that using the CFD tool captures secondary flow structures well, although CFD predictions are conservative.

Keywords: Experimental, Hot-wire anemometry, Outlet Guide Vanes, Turbine Rear Structure, Turbomachinery, Particle Image Velocimetry

Acknowledgments

First and foremost, my deepest gratitude goes to my supervisor Professor Valery Chernoray for all your support, ingenuity, attention to details and always taking the time for discussions and feedback. Isak Jonnson should also be mentioned for his support and valuable input in experimental work. I would like to thank the members of the AT3E/EATEEM projects working at GKN Aerospace Engine Systems. I would also like to thank faculty members, colleagues at the Division of Fluid Dynamics at Chalmers for a pleasant work environment. Last but not least, I also wish to express my gratitude to my family and friends.

Work in this thesis has received funding from: i) VINNOVA in the Swedish National Aviation Engineering Research Program (NFFP) through project AT3E, ii) the Clean Sky 2 Joint Undertaking under the European Union's Horizon 2020 Research and Innovation Program under grant agreement No 821398. Chalmers Laboratory of Fluids and Thermal Sciences is acknowledged for hosting the facility and the measurement equipment.

Valentin Vikhorev
Göteborg, December 2021

List of Publications

This thesis is based on the following appended papers & proceedings:

Paper 1 Valentin Vikhorev, Valery Chernoray, Oskar Thulin, Srikanth Deshpande, Jonas Larsson. *Detailed Experimental Study of the Flow in a Turbine Rear Structure at Engine Realistic Flow Conditions,* Journal of Turbomachinery, 143(9), 2021.

Paper 2 Valentin Vikhorev, Valery Chernoray. *Experimental Flow Analysis in a Modern Turbine Rear Structure with 3D Polygonal Shroud Under Realistic Flow Conditions,* Proceedings of 14th European Conference on Turbomachinery Fluid dynamics and Thermodynamics, 2021, ETC2021-539.

Paper 3 Valentin Vikhorev, Pär Nylander, Valery Chernoray, Jonas Larsson, Oskar Thulin. *Experimental and Numerical Flow Analysis of an Engine-Realistic State-of-the-Art Turbine Rear Structure,* Proceedings of ASME Turbo Expo 2021, GT2021-59224.

List of Acronyms

5HP	–	Five-hole Probe
7HP	–	Seven-hole Probe
BPR	–	Bypass Ratio
CFD	–	Computational Fluid Dynamics
HWA	–	Hot-wire Anemometry
LPC	–	Low-Pressure Compressor
LPT	–	Low-Pressure Turbine
MHP	–	Multi-hole Probe
NGV	–	Nozzle Guide Vanes
OGV	–	Outlet Guide Vanes
PIV	–	Particle Imaging Velocimetry
TRS	–	Turbine Rear Structure

Contents

Part I

Introductory chapters

Chapter 1

Structure of the Thesis

The thesis begins with a basic introduction and background of the work. This is followed by a section about conceptual design differences between baseline and state-of-the-art configurations of TRS. Aero-design of these two TRS configurations was done by GKN Aerospace Sweden. The following section explains the flow in a TRS and TRS functionality, including unpublished results from PIV and HWA experimental campaigns, focusing on inlet conditions and describing stator and rotor wakes coming from NGV and LPT. The subsequent summary of papers gives a brief review and discussion of the main results of appended papers as well as each author's contribution. Finally, ongoing and future work is discussed and appended papers are provided.

Chapter 2

Introduction

2.1 Background

The need to address the global challenge of CO_2 emissions from air transport, together with customer needs, pushes manufacturers and researchers to design and investigate new engine architectures that will deliver the best in the future of aviation. Therefore, engine components and configurations are under development in order to improve their mechanical, thermal, and propulsion efficiency.

One way to improve the propulsion efficiency is to increase the engine BPR, which can be achieved by a larger diameter fan and, therefore, larger volume of entrained air going through the bypass nozzle. However, the maximum tip fan velocity increases with a larger fan size. This, in turn, imposes limits on the rotational speed of the LPT and LPC coupled to the same shaft. Therefore, in a conventional design of a turbofan jet engine, to achieve the same efficiency requires extra turbine and compressor stages. The introduction of a gear system makes it possible to decouple the fan rotation rate and turbine rotation rate. As a result, the fan pressure ratios are lower, and all components can achieve their respective optimum speeds. Therefore, geared turbofan engines represent a major step forward in jet engine technology due to the significant boost of overall efficiency, lower fuel burn and carbon dioxide emissions, and weight and noise reduction.

New challenges are faced by engine component manufacturers. Due to the complexity of the engine and new imposed requirements, individual components should be optimized in terms of weight, aerodynamics, and total thrust. In order to maximize the thrust, it is important to maintain the flow that exits the LPT in an axial state. The flow straightening function is performed by a TRS comprised of OGVs, see Fig. 2.1, that serve to turn the flow, making it axial, as the flow exits the engine.

In addition, the TRS also serves a structural function by supporting a rear shaft bearing and connecting the engine core to the aircraft body. Thus, the OGVs positioned between the outer and inner TRS rings also perform a mechanical function and serve as structural connectors. Since the engine mounting relies on the TRS, the demands on TRS structural design are very high.

For this reason, TRS designers are following structural requirements and paying attention to the aerodynamic efficiency of components. The aerodynamic performance of a real TRS is affected by the OGV geometry, shape of rear engine mounts protruding into the casing, shape of a P-flange pocket, flow from the turbine, and complex end-wall geometries for the inner and outer TRS rings. These design variations can significantly influence the overall aerodynamic efficiency in terms of flow turning and pressure losses. Therefore, more detailed aerodynamic studies of TRS are needed to fully understand the influence of each of these parameters.

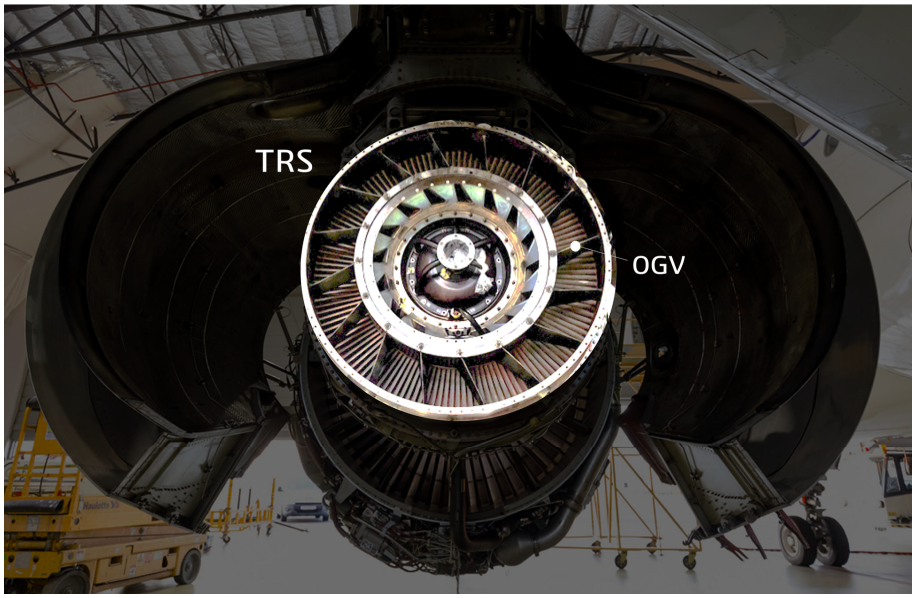

Figure 2.1: Rear view of geared turbofan CFM56 engine with highlighted TRS and OGVs. "CFM International CFM56-5B4", 2020, 'https://achtungskyhawk.com/2021/04/04/photo-file-you-spin-me-right-round-a-peek-at-the-cfm56/'. Reproduced with permission from the author Boran Pivcic.

2.2 TRS Designs

Modern TRS comprises OGVs of several different geometries. First, it includes vanes with enlarged thickness (so-called thick vanes) to provide a pathway for the inner oil supply line. However, large thickness of OGVs means greater pressure losses and therefore, such modifications should be designed in a way to minimize the latter. Moreover, for the consideration of strength and elimination of bending moments, modern TRS has bump vanes designed to protrude inner casing of TRS. Introduction of a bump vane can cause possible flow separations leading to larger pressure losses and corresponding lose in aerodynamic efficiency. Therefore, new challenges in terms of the design and aerodynamic performance should be met. The total number of OGVs, including regular vanes, has been determined by the structural requirements and weight reduction goal.

In this thesis, two configurations of TRS were experimentally investigated. Fig. 2.2 shows baseline and state-of-the-art configurations, representing two architectures of TRS that have been designed solely for the experimental rig and are not related to any GKN Aerospace product characteristics.

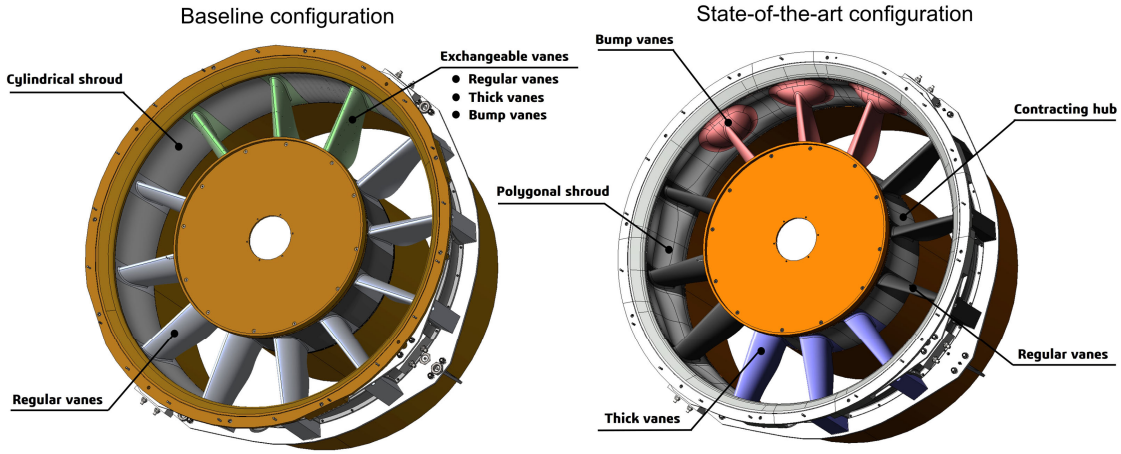

Figure 2.2: TRS architectures: (left) baseline configuration and (right) state-of-the art configuration.

For the baseline configuration, TRS with cylindrical shroud was equipped with nine regular vanes, and three exchangeable vanes of one of these types: regular, thick, or bump. Therefore, three sets of measurements were carried out. The measurements were performed on the mid-vane of the exchangeable vane sector. Two adjacent vanes in the sector provided periodic boundary conditions.

The second state-of-the-art configuration was equipped with six regular, three thick, and three bump vanes. All vanes were mounted simultaneously, reflecting engine realistic environment. Designs of vanes and end-wall geometries were optimized by GKN Aerospace, Sweden in terms of aerodynamic efficiency. In contrast to the baseline configuration, bump vanes were designed as one aerodynamic unit, while for the baseline configuration the bump part was designed separately and mounted on to the regular vane. The hub geometry was modified by making it contracting, as well as the shroud surface of TRS having a more complex three-dimensional polygonal shape. The main function of the polygonal shape is to increase the buckling resistance capability as well as reduce manufacturing cost, which becomes less due to a cheaper welding process for smaller panels.

2.3 Flow in TRS (including unpublished results)

The following section is related to flow aerodynamics including unpublished results from PIV and hot-wire measurements describing inlet flow structures originated upstream of the TRS. These measurements were done for the baseline configuration consisting of 12 regular vanes.

Fig. 2.3 shows schematic flow with superimposed oil visualization patterns, hot-wire, PIV, and total pressure contours for TRS section. The total pressure and swirl measurements were performed using pre-calibrated 5-hole and 7-hole aero probes (5HP and 7HP).

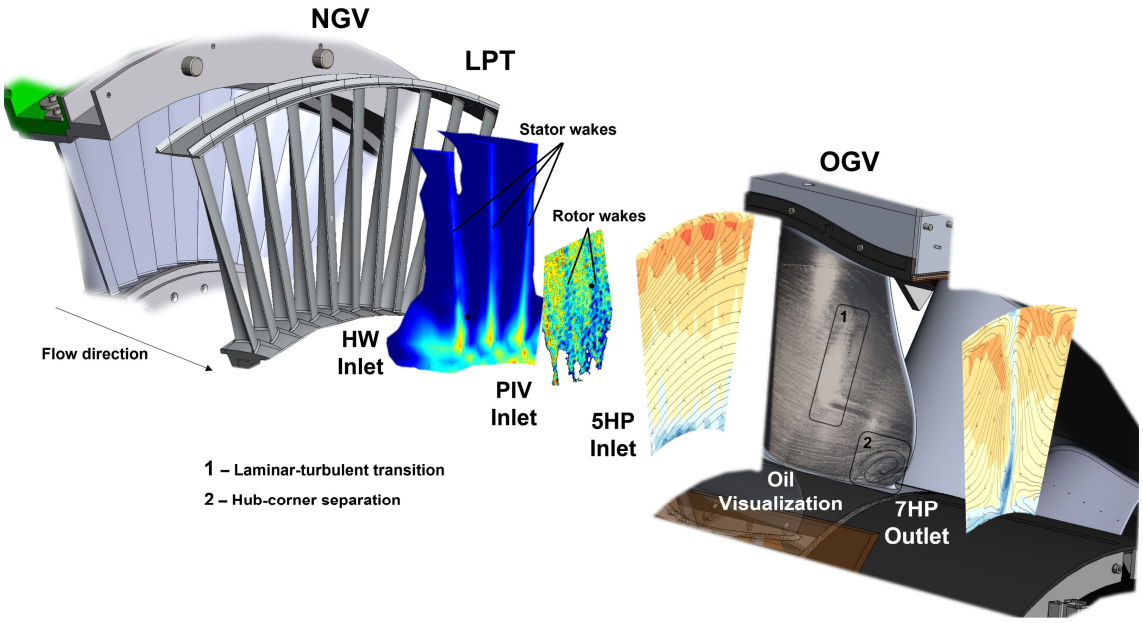

Figure 2.3: The TRS flow illustrated by oil visualization pattern, PIV, hot-wire and total pressure contours.

For diagnostics of an instantaneous flow upstream of OGV, a non-intrusive 3C-2D PIV measurement technique was used. The light-sheet optics for illumination and PIV cameras were located outside TRS. The seeding of the flow was done using a glycol-based fog generator. The images were postprocessed using 3C-2D PIV software from LaVision. Vector validation was performed by removing velocity vectors out of the expected range of velocities. Fig. 2.4 shows an instantaneous velocity field obtained from a cross section positioned 188 mm downstream LPT. The gray bounded area represents a projection of a TRS sector for reference. The PIV data presented here were obtained within the first PIV campaign conducted in the engine-realistic turbine facility at Chalmers. In the measured velocity field, one can clearly identify two LPT blade wake regions with a velocity deficit. As can be seen, rotor wakes originated from the LPT are composed of small-scale vortices no larger than 7 x 7 mm^2 in size.

To capture stator wakes and their downstream development, hot-wire measurements were done. A hot-wire probe was equipped with a tungsten wire of 3 mm active length and 5 μm in diameter. All measurements were performed with use of a traversing system moving the probe in a 3D space between the OGVs. Measured voltage data were converted into the velocity data using a calibration curve and then ensemble averaged over 30 blocks. Data is presented in the form of mean and standard deviation of ensemble averaged velocity (Fig. 2.5). The results from

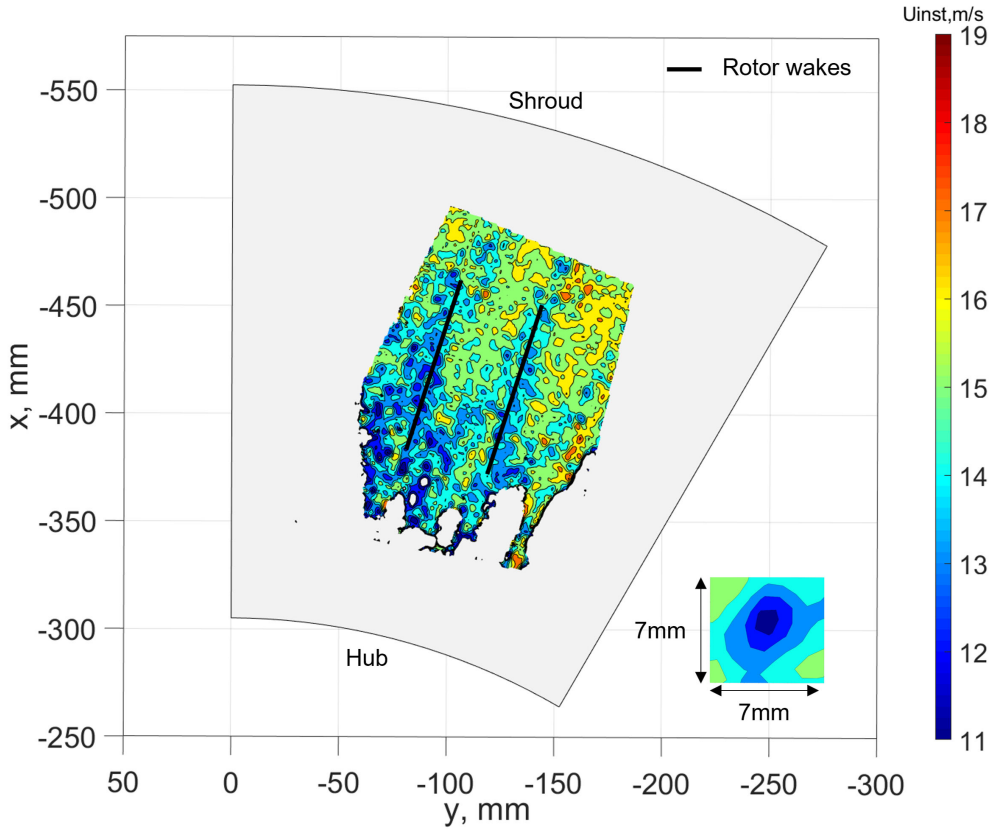

Figure 2.4: Instantaneous velocity flow field obtained from PIV measurements at axial location 188 mm downstream LPT.

standard deviation velocity contours (Fig. 2.5, right) clearly reveal three stator wakes inside the measurement volume. The downstream evolution of these wakes leads to a visible influence on the total pressure and affects the total pressure losses and total pressure redistribution in the TRS, as can be seen in the total pressure contours for inlet/outlet planes in Fig. 2.3.

The main aerodynamic purpose of OGVs is to efficiently turn the airflow. Fig. 2.6 presents circumferentially averaged profiles of swirl angle at inlet and outlet planes, showing good turning performance of TRS and therefore, the flow becomes almost axial. As seen from the inlet swirl angle profile distribution, the flow turning and thus the vane load are largest near the hub. As a result of the increased load, the flow diffusion is larger. Thus, the region with the low-momentum fluid close to the hub is very sensitive, requiring proper aero-design due to the (1) skewed velocity profile of the end-wall boundary layer in combination with (2) acting circumferential and radial pressure gradients with corresponding induced cross flow, and (3) adverse pressure gradient caused by the diffusion of the passage. For large mass flow rate conditions or low loaded vane, the development of the boundary layer in the hub corner does not lead to corner separations. However, increasing the swirl angle (more loaded vane) or lowering the mass flow rate can significantly affect the hub corner

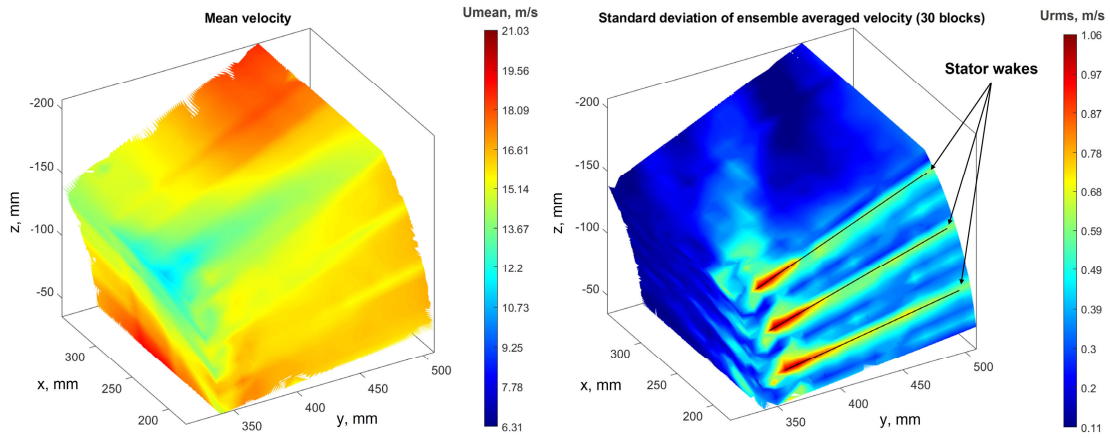

Figure 2.5: Ensemble averaged velocity in a 3D volume between OGVs using HWA technique: (left) mean and (right) standard deviation of ensemble averaged velocity.

region and introduce three-dimensional corner separation with reversal flow.

Furthermore, the formation of the secondary flows in the hub corner depends on the clearance between the turbine disc and TRS (so-called rim seal) and hub cavity flow. The interaction of the purge flow from the rim seal with the secondary flow in the TRS can influence the development of the hub boundary layer, and thus change the intensity of reverse flow. The purge flow can influence the total pressure and the swirl angle near the hub and hence the hub corner secondary flow structures.

The hub corner secondary flows account for a large part of the pressure losses from the TRS, adding to the losses from the boundary layers on wetted surfaces of OGVs, hub, and shroud.

The OGV boundary layer on the suction side is affected by the radial fluid migration and streamwise adverse pressure gradient. As a result, a separation bubble can occur. However, based on flow visualizations performed for investigated configurations at on-design case, the formation of the separation bubble was usually followed by laminar-turbulent transition and turbulent reattachment without notable contribution to pressure losses. For off-design cases, the flow separation led to additional losses from OGVs.

Thickening of the vane, as well as bump implementation, increases the diffusion and makes the corner areas more sensitive to separation problems. As was shown for baseline configuration, the bump was found to additionally affect the OGV aerodynamics indirectly by influencing the inlet conditions into the TRS with higher swirl angles, and by inducing additional losses in the near-hub region of the OGV. Aerodynamic study of the bump vane mounted in the state-of-the-art configuration does not reveal any substantial influence on the hub region for on-design case. For the bump vane, the flow in the shroud corner near the trailing edge is shown to have an additional, very diffused, boundary layer on bump surface and additional strong vorticity originating from the bump. Besides, combination of extra adverse pressure gradient due to the flow blockage and more loaded vane leads to reverse flow in hub

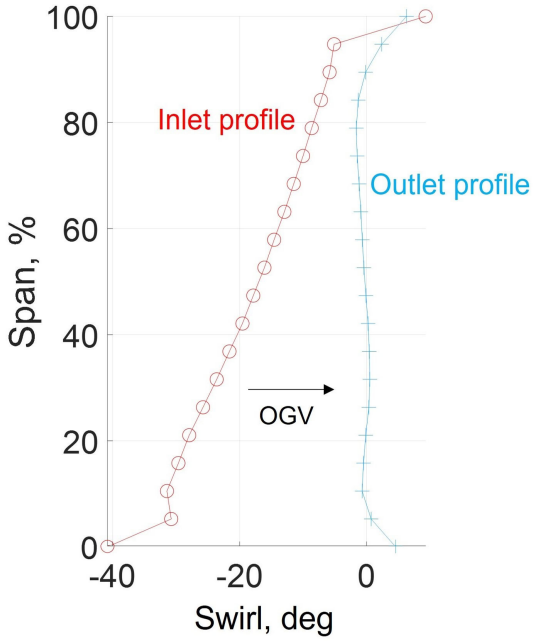

Figure 2.6: Circumferentially averaged profiles of swirl angle for TRS at inlet and outlet planes.

suction side corner. In contrast to the baseline configuration, the engine realistic TRS showed a different upstream influence of different vane types on inlet boundary conditions and, therefore, a conclusion was made that for an accurate aerodynamic evaluation all three vane types should be mounted simultaneously.

A successful aerodynamic design of TRS creates a need to study the flow in detail in order to correctly predict the TRS turning performance and loss production.

Chapter 3

Summary of Papers

Paper 1

Detailed Experimental Study of the Flow in a Turbine Rear Structure at Engine Realistic Flow Conditions.
Valentin Vikhorev (VV), Valery Chernoray (VC), Oskar Thulin (OT), Srikanth Deshpande (SD), Jonas Larsson (JL)

Division of Work

VV was the main author, performed pressure measurements and flow visualization, post-processed experimental data, and did the experimental analysis with further presentation of the paper at ASME Turbo Expo conference 2020. VC helped with instrumentation of TRS, data analysis, provided feedback on the paper, and supervised the work. JL gave aerodynamic analysis from the industrial perspective and provided feedback on the paper. OT coordinated the project and provided feedback on the paper. SD provided feedback on the paper.

Summary and Discussion

This paper contributes by providing experimental data for the flow in an annular TRS equipped with three types of outlet guide vanes typical for a modern TRS design: regular vanes, thickened vanes, and bump vanes with engine-mount recess. Total and static pressure measurements together with oil-film visualizations were performed in the annular LPT-OGV rig at engine-realistic inflow conditions. The measurements were performed at on-design and two off-design points varying ± 5 degrees from the on-design condition. The aerodynamic performance of each vane geometry has been investigated in detail. Comparison of thickened and regular vanes showed that mechanisms for the loss formation are similar for these two vanes, although thickening of the vane leads to higher pressure losses due to the increased blockage of the main flow and increased suction-side diffusion. The bump vane design is shown to have noticeable influence on downstream losses in the hub and shroud

regions, although the bump is shroud-located. As well, it was found that the bump vane affects the inflow conditions by influencing the inlet total pressure and swirl.

Contribution

The paper presents the first aerodynamic study in an annular TRS module with investigation of different OGVs typical for a modern aeroengine. Flow visualizations, combined with pressure measurements, provided data for quantitative analysis of secondary flow structures, and identified important areas where these structures contribute to pressure losses.

Paper 2

Experimental Flow Analysis in a Modern Turbine Rear Structure With 3D Polygonal Shroud Under Realistic Flow Conditions.
Valentin Vikhorev (VV), Valery Chernoray (VC)

Division of Work

VV was the main author, performed TRS instrumentation, pressure measurements and flow visualization, post-processed experimental data, and did the experimental analysis with further presentation of the paper at the 14th European Conference on Turbomachinery Fluid Dynamics and Thermodynamics. VC helped with data analysis, provided feedback on findings, and supervised the work.

Summary and Discussion

In this paper, aerodynamic analysis of an engine realistic state-of-the-art TRS with polygonal shroud containing several types of outlet guide vanes (regular, thick, and bump vanes) was performed. The aerodynamic study was undertaken for a fixed Reynolds number of 350,000 and three operation points. New design of the bump vane led to blockage with extra adverse pressure gradient that influenced the flow in the shroud region and additional vorticity region for all design cases. Blade- and bump-loading analysis shows the importance of design bump and vane as one aerodynamic unit. Wake comparison for different vanes shows that wake intensity does not significantly change for the on-design and low-loading conditions, while at the high-loading condition for the bump vane the hub region becomes more diffusive. For the bump vane, the oil-film visualizations indicate reversal flow and additional stagnation area in the shroud corner region. These two flow regions are the main suppliers of the additional pressure losses due to the bump.

Contribution

The present work is the first publication that provides aerodynamic evaluation of state-of-the-art TRS with 3D polygonal shroud geometry. Experimental data is

valuable not only from a fundamental perspective but also useful to the industry for further development of more efficient aeroengines.

Paper 3

Experimental and Numerical Flow Analysis of an Engine-Realistic State-of-the-art Turbine Rear Structure.
Valentin Vikhorev (VV), Pär Nylander (PN), Valery Chernoray (VC), Jonas Larsson (JL), Oskar Thulin (OT)

Division of Work

VV was the main author, performed pressure measurements and flow visualization, post-processed and compared experimental and numerical data, with further presentation of the paper at ASME Turbo Expo conference 2021. PN performed CFD simulations, helped with numerical data analysis and writing. VC helped with experimental data analysis, provided feedback on the paper, and supervised the work. JL gave valuable analysis from the industrial perspective, provided feedback on the paper, and helped with writing. OT coordinated the project and provided feedback on writing.

Summary and Discussion

This paper presents both experimental and numerical results for a state-of-the-art TRS with 3D polygonal shroud and simultaneously mounted regular, thick and bump vanes. The TRS performance was analyzed both at on- and off-design conditions. CFD was found to overpredict the intensity of the secondary flow near the hub on suction side and a vortex from a bump. Apart from this, CFD did not reveal a laminar separation bubble occurring at the on-design and high-load conditions. CFD showed good agreement with experiments for circumferentially averaged outlet profiles of the swirl angle, reflecting that the prediction of turning performance is very satisfactory. The investigation also showed that different vane types have different upstream influence, which is crucial knowledge for accurate modeling of TRS aerodynamics.

Contribution

The paper provides detailed side-by-side comparison of numerical and experimental results for state-of-the-art TRS considering the wakes, blade loadings, and flow visualization patterns. From numerical simulations it can be concluded that current CFD can be used as a conservative evaluation tool of TRS aerodynamic performance. Provided experimental flow analysis has significant value from the validation point of view.

Chapter 4

Ongoing and Future Work

The ongoing work includes heat transfer measurements on OGV and adjacent end-wall surfaces, which is crucial for thermal analysis of turbine rear structures and for assessing the heat transfer characteristics of the state-of-the-art design. Moreover, the leakage from the LPT rim seal will be added in order to study its impact on the flow and heat transfer. Another ongoing work is an investigation of the influence of manufacturing non-conformances on the TRS performance. For this purpose, a series of experiments with modelled welds on various TRS surfaces are conducted. In the next step, two additional TRS geometries with different number of OGVs and different lean angle will be investigated in the rig.

Part II

Appended papers

Paper 1

Valentin Vikhorev, Valery Chernoray, Oskar Thulin, Srikanth Deshpande, Jonas Larsson. **Detailed Experimental Study of the Flow in a Turbine Rear Structure at Engine Realistic Flow Conditions,** Journal of Turbomachinery, 143(9), 2021.

Valentin Vikhorev[1]
Department of Mechanics and Maritime Sciences,
Chalmers University of Technology,
Gothenburg SE-41296, Sweden
e-mail: valvik@chalmers.se

Valery Chernoray
Department of Mechanics and Maritime Sciences,
Chalmers University of Technology,
Gothenburg SE-41296, Sweden
e-mail: valery.chernoray@chalmers.se

Oskar Thulin
GKN Aerospace Engine Systems,
Trollhättan SE-46181, Sweden
e-mail: oskar.thulin@gknaerospace.com

Srikanth Deshpande
GKN Aerospace Engine Systems,
Trollhättan, SE-46181, Sweden
e-mail: srikanth.deshpande@gknaerospace.com

Jonas Larsson
GKN Aerospace Engine Systems,
Trollhättan SE-46181, Sweden
e-mail: jonas.larsson@gknaerospace.com

Detailed Experimental Study of the Flow in a Turbine Rear Structure at Engine-Realistic Flow Conditions

A good aerodynamic design of the turbine rear structure (TRS) is crucial for improving efficiency and reducing emissions from aero-engines. This paper presents a detailed experimental evaluation of an engine-realistic TRS which was studied in an engine-realistic rig at Chalmers University of Technology, Sweden. The TRS test section was equipped with three types of outlet guide vanes (OGVs) which are typical of modern state-of-the-art TRS: regular vanes, thickened vanes, and vanes with an engine-mount recess (a shroud bump). Each of the three vane geometries was studied under on-design and off-design conditions at a fixed flow Reynolds number of 235,000. The study shows that the off-design performance of the TRS strongly depends on the presence of the local flow separation on the OGV suction side near the hub, which is greatly affected by the vane pressure distribution and inlet conditions. Similarly, the OGVs with increased thickness and with a vane shroud bump are shown to affect the performance of the TRS by influencing the losses on the OGV suction side near the hub. Furthermore, the presence of the bump is shown to have a noticeable upstream influence on the outlet flow from the low-pressure turbine and a noticeable downstream influence on the outlet flow from the TRS. [DOI: 10.1115/1.4050451]

Keywords: computational fluid dynamics (CFD), fan, compressor, and turbine aerodynamic design, fluid dynamics and heat-transfer phenomena in compressor and turbine components of gas turbine engines, measurement techniques, low-pressure turbine, outlet guide vane, turbine rear structure, engine exit structure, turbine exhaust casing, tail bearing housing, turbine rear frame, exit guide vane, engine-mount recess

1 Introduction

Near-future demands for the reduced environmental impact of air transport have stimulated the innovation and improvement of the air engine design. The aerospace industry needs to meet the goals set by the Advisory Council for Aeronautics Research in Europe for the year 2050, where the main targets are a 75% reduction in CO_2 emissions, a 90% reduction in NO_x emissions, and a 65% reduction of the perceived noise relative to engine and aircraft performance compared to values of the year 2000. In line with these requirements, increased bypass ratio (BPR) turbofan engines with ultra-high efficiency are currently under development. A prerequisite of the ultra-efficient engine design is careful aerodynamic and weight optimization of each engine component.

The larger fans of high-BPR engines require larger power and lower rotational speeds, which imposes new conditions on the aerodesign of the low-pressure turbine (LPT) and turbine rear structure (TRS). The TRS is a structural stator stage downstream of the LPT, which de-swirls the flow after the LPT to maximize engine thrust. The TRS consists of outlet guide vanes (OGVs), and a modern TRS includes several vane types: regular vanes, vanes equipped with an engine-mount recess (shroud bump), which serve a structural purpose, and vanes with increased thickness to allow for the passage of the bearing oil tubes.

In a traditional two- and three-spool engine, the increased BPR results in a highly loaded LPT and large swirl angles out of the last LPT rotor. In a geared engine with a high-speed turbine decoupled from the fan the outlet swirl angle from the turbine rotor is less problematic. However, the off-design variations of the outlet swirl angle increase substantially. Both factors make the aerodynamic design of a modern TRS more demanding, and a robust TRS design that performs well for all engine operating points is therefore particularly challenging.

The flow in the TRS is highly diffusive with the interaction between the boundary layers of the OGVs with the boundary layers of the hub and shroud and with a swirled unsteady incoming flow from the LPT. The interacting decelerated boundary layers in combination with the adverse pressure gradient lead to local flow separations. The prediction of these flow separations is particularly challenging since the boundary layers on OGVs undergo laminar-turbulent transition. Both the laminar-turbulent transition and flow separation are challenging for numerical predictions using computational fluid dynamics (CFD) simulations. Therefore, detailed experimental aerodynamic and heat-transfer studies of the TRS under on-design and off-design conditions are required.

The first detailed aerodynamic studies of OGVs were made in a linear LPT-OGV cascade, representing a two-dimensional approximation of vanes without a curvature effect, radial pressure gradient, and unsteady turbine wakes. A significant contribution to the research field was made by Hjärne et al. [1–3]. Besides the experimental results for on- and off-design conditions, these studies presented validation of numerical simulations. In further works by Hjärne et al. [4,5] detailed the investigation of the secondary flows and loss development was performed experimentally and numerically noting the effect of the free-stream turbulence and inlet boundary layer thickness on the secondary flows. The study of the TRS in an annular rig with an unshrouded turbine was performed by Selic et al. [6]. This work highlighted the effect of the turbine tip clearance on the losses and the importance of an

[1]Corresponding author.

Proceedings of the ASME 2020, Turbomachinery Technical Conference and Exposition, GT2020, June 22-26, 2020, London, England, GT2020-15734.

Contributed by the International Gas Turbine Institute (IGTI) of ASME for publication in the Journal of Turbomachinery. Manuscript received November 14, 2020; final manuscript received February 3, 2021; published online May 12, 2021. Tech. Editor: David G. Bogard.

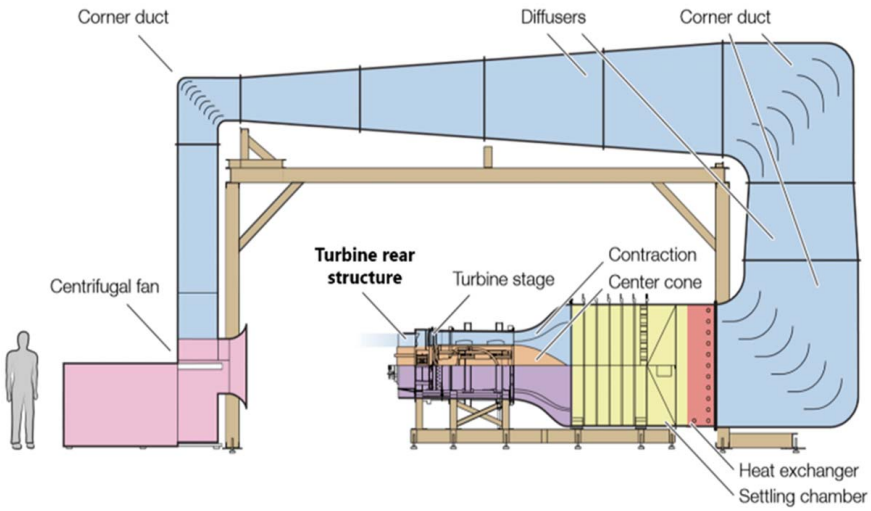

Fig. 1 Section view of the LPT-OGV facility [8]

engine-realistic LPT stage. Further investigations in a newly established TRS facility at Chalmers University of Technology [7–9] were carried out in a rig equipped with a realistic shrouded LPT and operated at engine-realistic flow Reynolds numbers. The design of the new rig is presented by Rojo et al. [7]. Jonsson et al. [8] presented the accurate measurements of the heat-transfer coefficient on OGVs, which has allowed for the mapping of the laminar-turbulent transition on OGVs for a number of aerodynamic load cases, and his work is further extended and compared to CFD in an accompanying paper [10]. Jonsson et al. [9] illustrated the impact of surface roughness on secondary flows and pressure losses in a TRS. Both studies [8,9] highlighted the significance of the laminar-turbulent transition on the performance of the TRS.

The studies [7–9] were performed for TRS consisting of 12 so-called regular vanes; however, a typical modern TRS design includes several (two or more) vanes equipped with an engine-mount recess (also called a shroud bump) and several (typically two–three) thickened vanes. The role of the engine-mount recess is to structurally enforce the TRS at the attachment points of the engine to the aircraft. The role of the thickened vanes is to provide space for oil tubes lubricating the rear engine bearings. The influence of the bump vane was previously studied in a linear cascade [11], but neither the bump nor the thickened vane has previously been studied in an annular rig with an upstream LPT. The aim of the current study is to investigate the performance of a realistic TRS with the implementation of the thick and bump vane under on- and off-design conditions.

2 Experimental Details

Experimental investigations were carried out in a closed-circuit low-speed large-scale 1.5 stage LPT-OGV facility at Chalmers University of Technology, Sweden. Figure 1 presents the schematic diagram of the facility. Operating conditions for the TRS that can be achieved in the rig are realistic for up to large turbofan engines with Reynolds numbers of up to 435,000 and above. The airflow is driven by a 250-kW centrifugal fan. The flow from the centrifugal fan passes through diffusers and corner ducts, which are equipped with turning vanes, and enters the settling chamber containing a honeycomb and five dampening screens of different sizes, from larger to smaller size meshes. The settling chamber enables uniform flow into the contraction and reduces the turbulence level. The steady temperature of the flow is maintained by a heat exchanger enabling steady flow conditions in the rig with good repeatability.

The LPT stage consists of a stator stage with 60 nozzle guide vanes (NGVs) and a shrouded rotor stage with 72 blades and is a research LPT geometry designed by GKN Aerospace Engine Systems, Sweden. The LPT stage provides realistic inlet boundary conditions for the TRS section. The TRS includes 12 OGVs which are positioned with a 30-deg spacing. A hydraulic brake on the turbine's rotor shaft provides a well-controlled load for the turbine. The turbine braking torque and the axial velocity in the test section are controlled in order to obtain constant values of the flow Reynolds number and the flow coefficient (FC), defined as the ratio of the axial velocity to the blade speed

$$FC = U_x/V \tag{1}$$

Further details of the facility design are provided by Rojo et al. [7].

The TRS section is equipped with two internal traversing systems working independently, moving radially and circumferentially. The traversing system located downstream of the TRS has an additional axial stage enabling a probe to be positioned at any point within the TRS. The traversing systems are fully automated and controlled by a personal computer (PC) with in-house LABVIEW® (National Instruments Corporation, Austin, TX) software scripts. The positioning accuracy in the circumferential directions is 0.01 deg and in the radial and axial directions 0.075 mm.

Total pressure and swirl measurements are performed using pre-calibrated five-hole and seven-hole aero-probes on two planes, one located upstream (inlet plane) and one downstream (outlet plane) (Fig. 2). Static pressure measurements on the vane and shroud bump were taken with the help of two Scanivalve mechanical

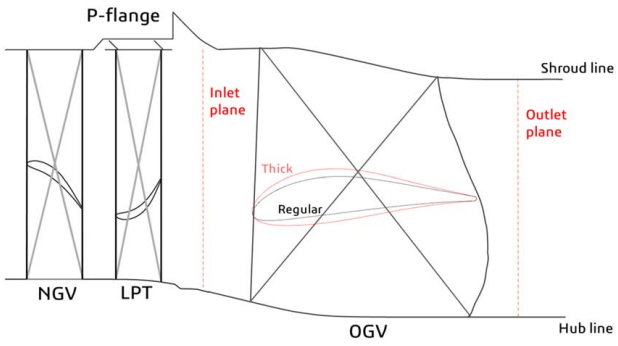

Fig. 2 Meridional view of turbine stage and test section, illustrating measurement planes and mid-span blade profiles

multiplexers with 48 ports each. The pressures from the multi-hole pressure probes and Scanivalve multiplexers are acquired using a 16-channel PSI-9116 system with a 500-Hz sampling rate and 2.5-s sampling time.

The total and static pressure data are presented in the form of non-dimensional coefficients (Eqs. (2) and (3)). The reference values are measured by a stationary Prandtl tube located in the bulk flow region between OGVs at 0.7 chord distance from the leading edge

$$C_{p0} = \frac{P_t - P_{tref}}{P_{tref} - P_{sref}} \tag{2}$$

$$C_p = \frac{P_s - P_{sref}}{P_{tref} - P_{sref}} \tag{3}$$

Tests are carried out under on-design and off-design conditions. The flow Reynolds number based on inlet channel height is 235,000, which is used for all three operation points. The TRS inlet conditions are summarized in Table 1 where the flow coefficient values are presented with their corresponding averaged LPT exit swirl angles.

Tests are performed for three types of TRS vanes: a regular vane, a thick tube vane, and a vane equipped with an engine-mount bump. It shall be noted that the LPT and TRS components have been designed solely for the experimental rig and are not related to any GKN Aerospace product characteristics.

For the regular vane configuration, the test section was equipped with 12 regular vanes, and for two other configurations, the test section was equipped with three modified vanes and nine regular vanes. The measurements were performed on the mid-vane of three modified vanes.

2.1 Thick Vane. The requirement of allowing oil pipelines to pass through OGVs leads to the increased thickness of the OGVs. A dedicated tube vane (research configuration) with enlarged thickness was designed by GKN Aerospace Engine Systems. Compared to the regular research OGV, the mid-span airfoil section of the thick OGV has an increased thickness by 45% (Fig. 2) while the camber line is maintained the same.

Figure 3 depicts a 3D model of a thick vane manufactured with stereolithography (SLA) rapid prototyping method.

Three thick vanes were implemented in the rig to reflect conditions in a real aero-engine. The aerodynamic performance of the vanes was evaluated according to the measurement of total pressure and flow angles at inlet and outlet planes. The static pressure distribution on the vane was monitored via pressure taps with a diameter of 0.7 mm, which were embedded in the OGVs. The static pressures were measured at five spans on the vane: at 12.5, 25, 50, 75, and 87.5%. Two instrumented vanes were manufactured, one equipped with pressure taps at 12.5, 50, and 87.5% spans and one equipped with pressure taps at 25, 50, and 75% spans. Figure 3 shows one of the vanes. These vanes were swapped one by one in the location of the measurement vane. The mid-span pressure taps were present on both vanes and were used to check the repeatability of the measurements.

Table 1 Inlet conditions

Operating condition	Flow coefficient, *FC*	Inlet swirl angle, deg	Re
On-design	0.622	−16.5	235,000
Off-design (low loading)	0.588	−11.5	
Off-design (high loading)	0.657	−20.9	
Off-design (high loading)	0.775	−31.6	

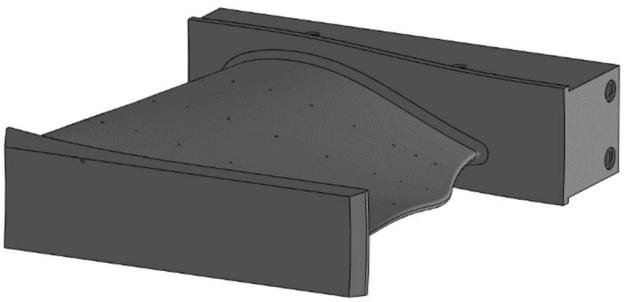

Fig. 3 A 3D model of a thick OGV (so-called tube OGV) with implemented pressure taps

2.2 Bump Vane. The engine mounts by which the aero-engine is mounted to the aircraft are attached to the TRS. To reduce induced bending moments, a structural engine-mount recess is provided on the TRS shroud, where the engine mounts are attached. The engine-mount recess results in a bump protruding into the gas path of the TRS. A research configuration of the OGV with an engine-mount bump on the shroud was designed by GKN Aerospace Engine Systems. Figure 4 shows a 3D model of the studied bump vane.

Three vanes with engine-mount bumps were implemented in the rig to reflect conditions in an aero-engine. A mid-vane of the three vanes was equipped with pressure taps on the vane and the bump. The two other bump OGVs were made from regular OGVs by adding bump modifications to the shroud. The pressure taps on the vane surface were positioned along three spans (25, 50, and 75%) and the distribution of the pressure taps on the bump surface is shown in Fig. 4. The bump surface was equipped with 96 pressure taps.

3 Results and Discussion

The experimental results are presented in four subsections according to the type of data. The emphasis of this article is on the comparison of the aerodynamic performance of the thick vane and bump vane with the regular vane. Thorough aerodynamic studies, as well as numerical investigation of the TRS with regular vanes, are provided by Jonsson et al. [8,9] and Arroyo [12].

3.1 Flow Visualizations. The objective of this section is to highlight the flow behavior around the OGV for different operating conditions. An oil-film visualization of the OGV suction side was

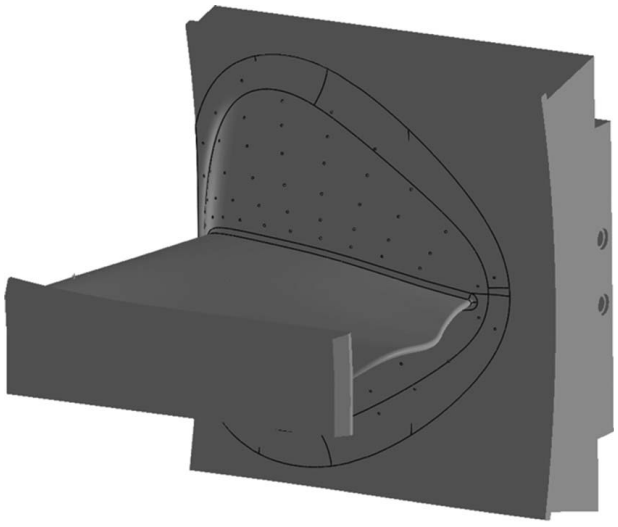

Fig. 4 A 3D model of the OGV with an engine-mount recess (bump) and implemented pressure taps on the bump surface

carried out to visualize the near-wall streamlines and flow separations. The thick OGV oil visualizations are presented in this paper. Similar visualizations for the regular OGV are provided by Jonsson et al. [10].

The visualizations were performed by the oil-film method. A mixture of kerosene, mineral oil, and TiO_2 powder, with particles from 0.2 to 0.3 μm, was used.

The visualizations (Fig. 5) demonstrate clear changes in the surface streamlines with changes in the flow coefficient. In all shown cases, one can observe that the flow on the vane near the hub and shroud migrates toward mid-span, which creates two deceleration zones in the endwall regions due to the area expansion of the stream tubes.

At minimal OGV load (see Fig. 5(*a*) at the off-design flow coefficient 0.588), the near-wall streamlines are smooth without any indication of flow separation. For the on-design condition (Fig. 5(*b*)), a small region with accumulated particles is clearly visible at the OGV trailing edge near the hub, indicating a very small local separation bubble with reattachment. This is most likely caused by the secondary flows from the hub migrating up along the vane suction side. Furthermore, a streamline deviation in the design point with flow coefficient 0.622, marked with blue dashes in Fig. 5(*b*), is visible near the hub at 25% span and approximately 40% chord. The authors believe that this is caused by a local laminar separation bubble followed by transition and turbulent reattachment. The flow deceleration near the hub increases at increased vane loads (Figs. 5(*c*) and 5(*d*) at the off-design flow coefficients 0.657 and 0.775, respectively). A growing region with reversed flow near the OGV trailing edge close to the hub is formed as the load increases. At the off-design case with flow coefficient 0.657 (5-deg higher absolute swirl), shown in Fig. 5(*c*), there is a mid-span region with accumulated oil particles at ~40% chord, highlighted by a blue dashed line. This region disappears at increased vane load as shown in Fig. 5(*d*). It was found that the formation of this region is very sensitive to the oil-film thickness, which indicates that a laminar flow separation with further turbulent reattachment may take place. The accompanying study [10] shows that on the regular vane, the laminar-turbulent transition of the boundary layer takes place in this location and that the transition occurs at strong negative values of the acceleration parameter close to the separation margin.

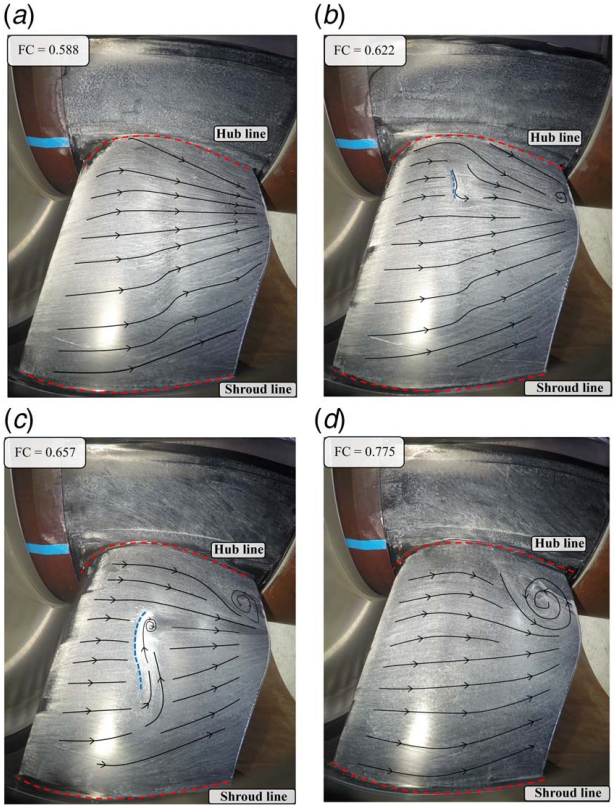

Fig. 5 Oil-film visualizations on a thick OGV suction side at on-design flow coefficient ((*b*) 0.622) and three off-design flow coefficients ((*a*) 0.588, (*c*) 0.657, and (*d*) 0.775) (Color version online.)

3.2 Pressure Load Distribution on the Vanes and Bump.

Figure 6 presents static pressure coefficients for the regular and thick vanes at on-design conditions for 25, 50, and 75% spans.

The thick vane has a larger blockage than the regular vane. This yields increased acceleration and lower static pressures both on the suction side and on the pressure side. This can be seen on all spans as shown in Fig. 6. The minimum pressure, on the more critical suction side, is reduced for the thick vane. This increases the diffusion and makes the thick vane more sensitive to separation problems. The axial position of the suction minimum does not change notably between the regular and the thick vanes.

For both vanes, however, the suction peak moves downstream as the span increases. Since both vanes have been designed with similar camber-lines and scaled thickness distributions, this similarity is expected. A kink can be observed at approximately 40% chord, which typically indicates a laminar flow separation. The location of this kink is consistent with the flow visualization results (Fig. 5(*b*)).

The pressure load of the thick vane, when compared to the regular vane, obviously increases at all spanwise locations. The pressure load is characterized by the area restricted between the pressure side and the suction-side curves according to the pressure force definition. As known from the force balance in the two-dimensional cascade theory, the lift force on the vanes is coupled with the flow turning through the cascade; however, this is not necessarily the case for 3D vanes due to the spanwise flow redistribution.

Figure 7 presents a comparison of the static pressure coefficient distributions for the regular and bump vanes at on-design conditions for 25, 50, and 75% spans. Notably, for 25 and 50% spans, the vane load change is minor. A slight pressure coefficient decrease is observed which can be explained by the presence of a bump as a blockage to the passing flow. However, for the spanwise location near the shroud (75% span), which is located closest to the bump, the changes are significant, due to the promoted acceleration of the flow in the front part of the bump and promoted deceleration in the rear part of the bump. As a result, the suction-side pressure peak on the vane near the bump (75% span) is moved upstream.

A side-by-side comparison of the pressure distributions for the thick vane and the bump vane in Figs. 6 and 7 shows that the near-hub region at 25% span and the mid-span region at 50% span are affected more by the increased vane thickness than by the bump.

Figure 8 presents the static pressure coefficient distributions on the bump surface under on-design conditions. Figure 8(*a*) shows the data at actual measurement points, and Fig. 8(*b*) shows the interpolated data.

There is a high-pressure region in front of the bump caused by the flow stagnation, which is followed by a low-pressure region in the region of the maximum bump thickness. The bump pressure distribution interacts with the vane pressure distribution resulting in the negative pressure on both vane sides, which also explains the pressure distribution of Fig. 7(*c*). The pressure minimum on the vane suction side is located at 25% chord and on the vane pressure side at 10% chord.

The pressure distributions on the bump at other inlet swirl angles did not show a notable difference. The pressure distributions on the bump do not indicate any flow separation on the bump, which points to a good aerodynamic performance for the current aerodesign of the bump itself.

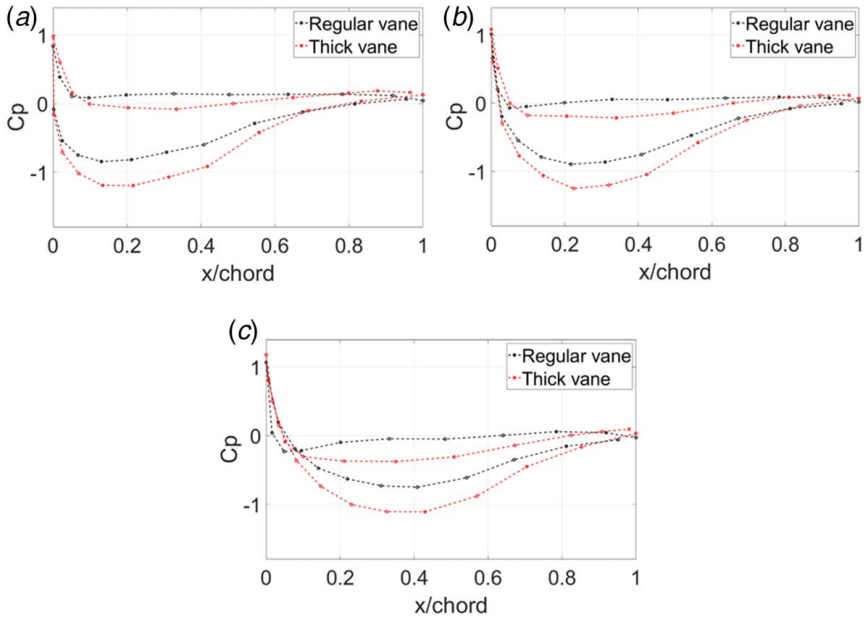

Fig. 6 Static pressure coefficient distributions at (*a*) 25, (*b*) 50, and (*c*) 75% spans for the regular and thick vanes at on-design flow coefficient

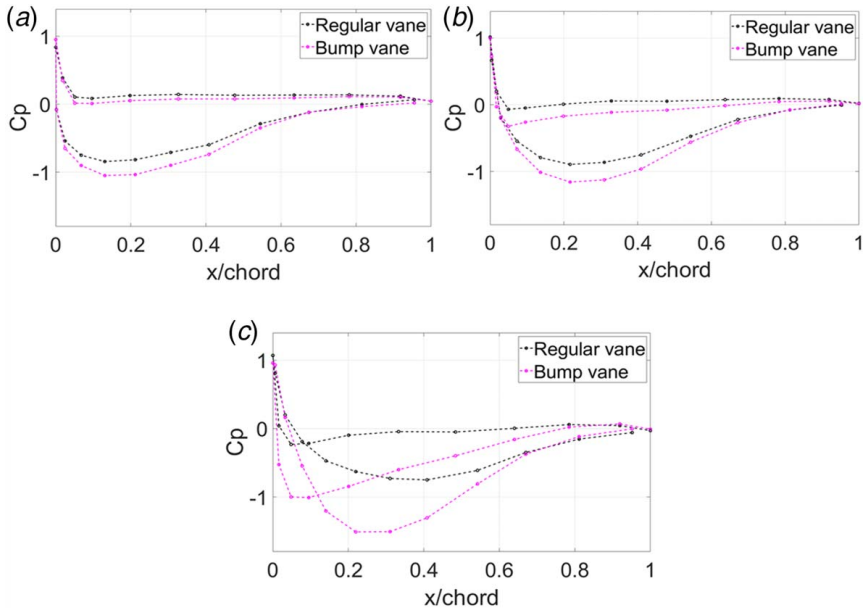

Fig. 7 Static pressure coefficient distributions at (*a*) 25, (*b*) 50, and (*c*) 75% spans for the regular and bump vanes at on-design flow coefficient

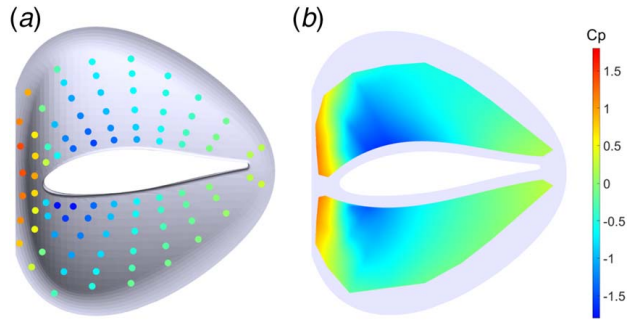

Fig. 8 (*a*) Static pressure coefficient (C_p) and (*b*) interpolated C_p distributions on the bump at on-design flow coefficient

The distributions of the static pressure coefficient at mid-span for the regular, thick, and bump vanes at all three operational points are presented in Fig. 9.

The change of the flow coefficient leads to a notable change in the vane load, as expected. The increase of the flow coefficient for all vane types moves the minimum pressure point on the suction side toward the leading edge. In addition, with the increase of the vane load, a kink appears in the deceleration region at the suction side, at ~40% chord, which indicates the presence of a local laminar flow separation followed by transition and reattachment for all three vane types.

To summarize all static pressure data, contours of the static pressure coefficient on the suction side of the regular, thick, and bump vanes at on- and off-design conditions are presented in Fig. 10. For the thick vane, the data show extra spans, which were not shown

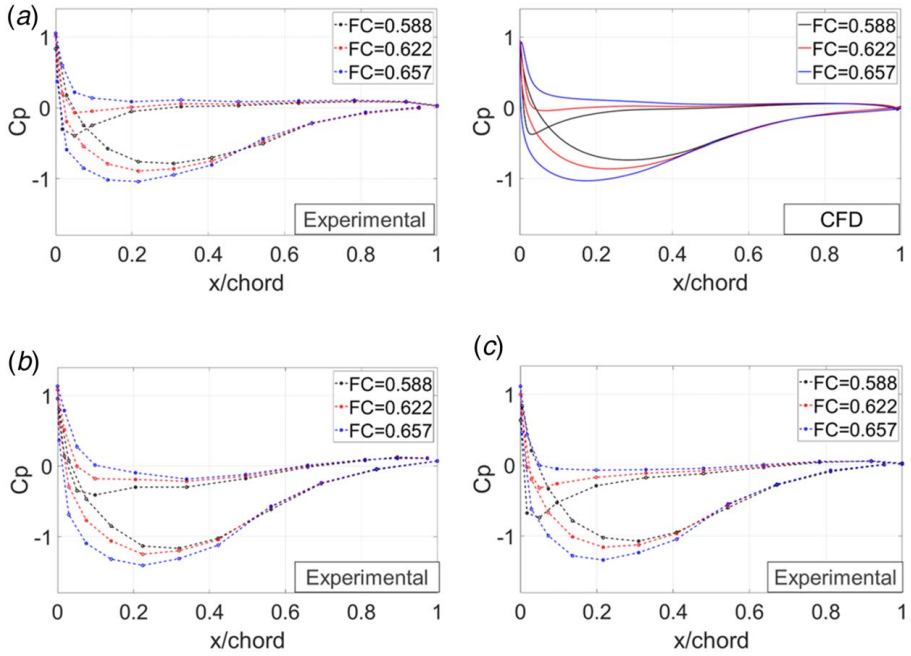

Fig. 9 Static pressure coefficient distributions at mid-span of the (*a*) regular, (*b*) thick, and (*c*) bump vanes under on- and off-design flow coefficients

previously, close to the hub at 12.5% span and close to the shroud at 87.5% span.

The static pressure contours once more illustrate that the vane thickening affects the pressure along the entire OGV span while the bump, as expected, has the largest effect near the shroud. The effect then gradually decreases toward the hub. Furthermore, the pressure distributions show that both thick and bump vanes are robust and handle off-design angles well. The position of the stagnation point does not change for the different vane types.

3.3 Inlet and Outlet Measurements. This section presents the total pressure and swirl angle measurements at the inlet and outlet of the TRS. The measurements were performed in 30-deg sectors upstream and downstream of the OGV.

Figure 11 presents the total pressure coefficient distributions at the inlet plane for all three vane configurations at the on-design point. The streamlines in the figure show the crossflow velocity components.

Traces of stator wakes can be seen for all three vane types in Fig. 11. These wakes originate from the NGV's upstream of the LPT rotor. Further, the local total pressure drop regions near the hub should be noted. These local loss regions originate from secondary flow vortices from the NGVs. Further details of their origin are provided by Arroyo [12].

Figure 12 shows the inlet circumferentially averaged swirl and total pressure coefficient profiles for the different vanes under on-design and two off-design conditions.

An interesting observation is that there is an inlet swirl variation across the channel. The flow swirl on the vane is the largest (the absolute value of swirl angle is the largest) near the hub and decreases near the shroud where it reaches zero and positive swirl angle. As a result, the vane load is the largest near the hub. Notably, in comparison with other cases, the inlet swirl angle for the bump vane case decreases near the hub (thus, the load increases) due to the upstream influence of the bump vane (Fig. 12(*a*)). The inlet total pressure profile (Fig. 12(*b*)) is skewed as well, with the lowest total pressure near the hub and the largest in the shroud region. Importantly, with the increase of the flow coefficient, the skewness of the total pressure profile decreases. For different vane cases, the total pressure profile skewness changes as well, with the thick vane case having the least skewed profile and the bump vane case having the most skewed profile.

Figure 13 shows the comparison of the total pressure coefficient for the regular, thick, and bump vanes at on-design and two off-design points at the outlet of the TRS. Figure 14 shows the CFD results for regular vane at on- and off-design flow coefficients.

As seen, the shape and intensity of the wake for the thick vane are similar to those of the regular vane, which suggests that the mechanisms for the loss formation are similar for these two vanes. As the flow visualizations of Fig. 5 show, the flow from the endwalls on the suction side of the vane is directed toward the midspan, due to the combined effect of the endwalls and the pressure gradient in the cascade between the pressure and the suction sides [13]. Since the load of the OGV is the largest near the hub and the total pressure is the lowest, a region with the lowest total pressure is formed from the OGV suction side near the hub. The endwall influence near the shroud also leads to the formation of a low total pressure region, which is less pronounced since the inlet total pressure is larger near the shroud and the vane load is smaller. The thickening of the vane leads to a slight increase in losses in the near-hub region (Figs. 13(*d*)–13(*f*)).

The presence of the bump on the OGV is notably redistributing the total pressure in the shroud region. Further, the total pressure near the hub is visibly larger due to the more skewed inlet total pressure profile. Moreover, the region with the increased losses near the shroud is moved from the OGV wake toward the shroud, due to the action of the bump. Additionally, it is seen that at flow coefficient 0.588, the losses in the OGV wake are very similar to the regular and thick vane cases; however, there is an additional region with the increased pressure loss created near the hub, which indicates a possible flow separation on the hub wall due to the extra adverse streamwise pressure gradient induced by the bump. At increased flow coefficient, this region increases and merges with the high-loss region on the vane suction side near the hub, creating a common loss region. The total pressure losses are visibly larger in this region when compared to the regular and thick vane cases.

Figure 15 shows the circumferentially averaged downstream profiles of the swirl and total pressure for the different vanes under an on-design and two off-design conditions. Figure 15(*a*) shows that

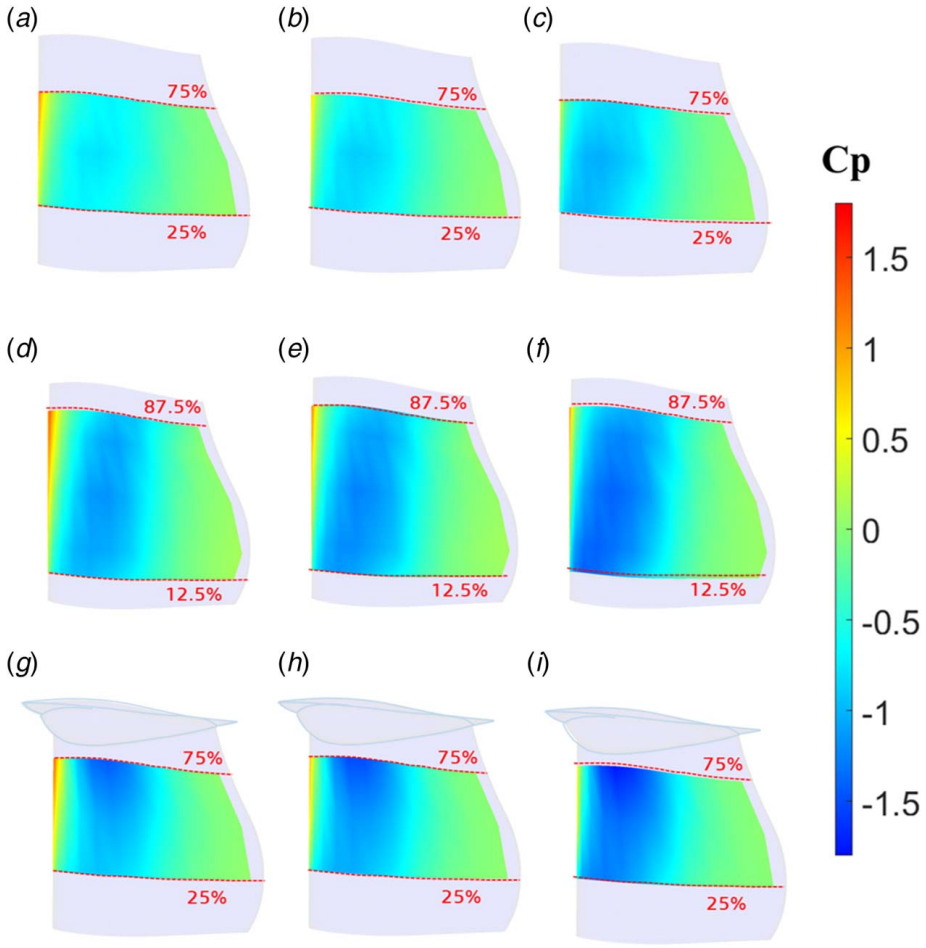

Fig. 10 Contours of static pressure coefficient on the suction side of the regular: (*a*) FC = 0.588, (*b*) FC = 0.622, and (*c*) FC = 0.657; thick: (*d*) FC = 0.588, (*e*) FC = 0.622, and (*f*) FC = 0.657; and bump: (*g*) FC = 0.588; (*h*) FC = 0.622, and (*i*) FC = 0.657 vanes at on- and off-design flow coefficients

the regular and thick vanes have very similar outlet swirl profiles. Both vanes are overturning the flow at flow coefficient 0.588, when the vane load is larger, compared to the on-design case of 0.622, and underturning the flow at flow coefficient 0.657. The underturning and overturning are less than by 1 deg as aimed by the vane design. For the bump vane, the flow turning is visibly increased in the hub region and decreased in the shroud region. Figure 15(*b*) shows that near the hub the losses are the largest at flow coefficient 0.657 and the smallest at flow coefficient 0.588. The regular vane and the thick vane have very similar losses, but the bump vane shows substantially increased losses in the hub region.

3.4 Comparison of Outlet Wake Profiles. Figure 16 presents the total pressure coefficient for the thick and bump vanes in the spanwise locations near the hub compared to the regular vane at the on-design point.

As can be seen from the wake profile of the thick vane, a change in the blade thickness does not lead to a change in the pressure loss. This supports the previous conclusions that the thickening of the vane does not affect the flow in terms of the aerodynamic performance for the on-design case compared to the regular vane.

Significant changes in the wake thickness are seen for the bump vane case. As the presented profiles show, the wake thickness and depth are significantly increased at the span closest to the hub (12%). At 25% span, the increase is less, and at 32% span, the wakes are nearly identical in strength.

Figure 17 shows the wake profiles at different spans for the two off-design cases. These results demonstrate that for the thick vane, the flow becomes more sensitive in the hub region for decreased values of the flow coefficient. This translates to the enlargement of the wake depth. For both off-design flow coefficients at 12% span, the wake increases about twice for the bump vane compared to the regular and thick vanes. At 25% span, the wake increase is less, and at 32% span, the wake increase is negligible. Thus, the additional losses are created in the near-hub region as discussed. Increased flow coefficient leads to increased wake size in the near-hub region as well, and the profile losses (losses due to the boundary layers near the midspan) are not greatly affected.

3.5 Initial Computational Fluid Dynamics Results. Initial comparisons with numerical CFD predictions have been done for the regular vane; 3D steady-state CFD simulations were performed for one TRS vane sector using FluentTM v19.1. A resolved multi-block structured mesh with $\sim 2 \times 10^6$ cells and $y^+ < 1$ was created in ICEM HexaTM. Simulations were performed using the SST k–ω turbulence model and the Langtry–Menter γ–Θ transition model [14]. CFD predictions of the pressure distributions, as shown in Fig. 9, agree very well with the experimental results. CFD wake profiles are shown in Fig. 14 and agree well for the low-load and ADP cases (FC, 0.588 and 0.622). In the more loaded case (FC, 0.657), CFD predicts a bit too large separation around the 25% span region. This confirms previous experience that the SST k–ω model is a bit conservative in terms of separation predictions.

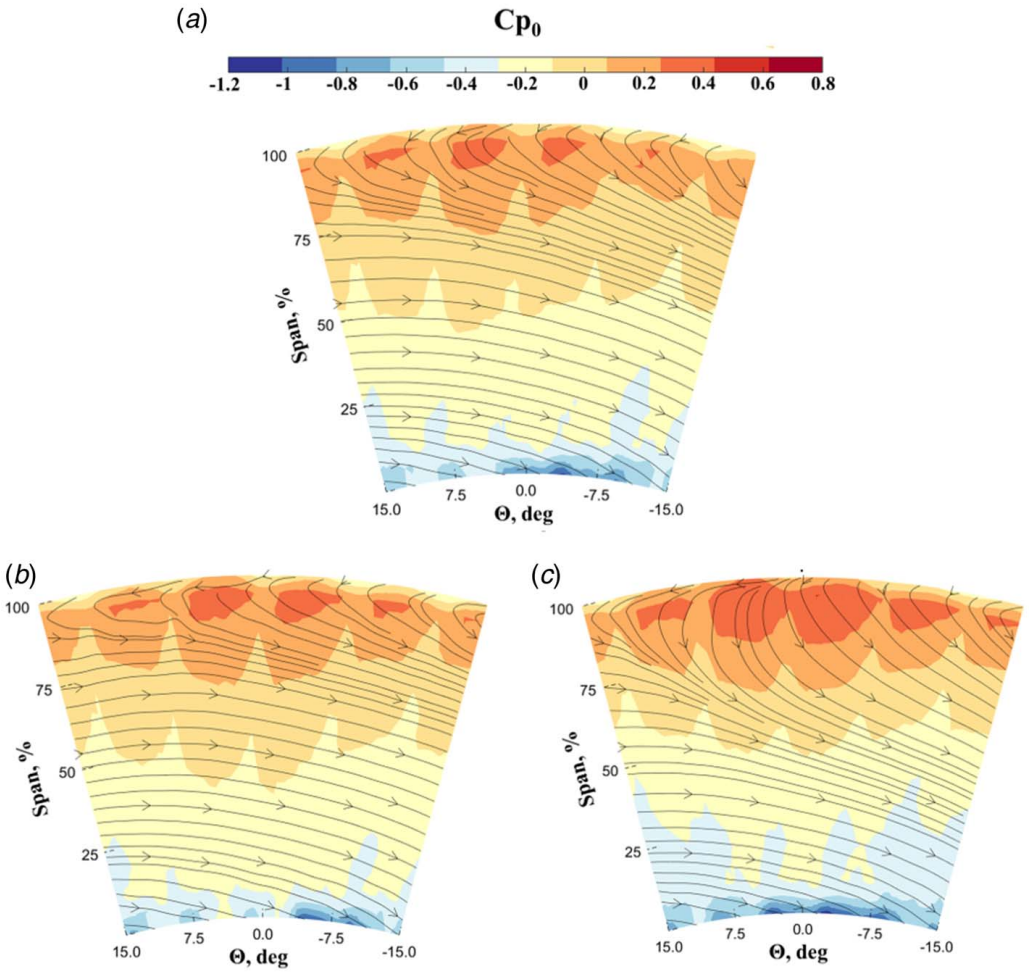

Fig. 11 Total pressure coefficient distributions at inlet plane for (*a*) regular, (*b*) thick, and (*c*) bump vanes at on-design flow coefficient

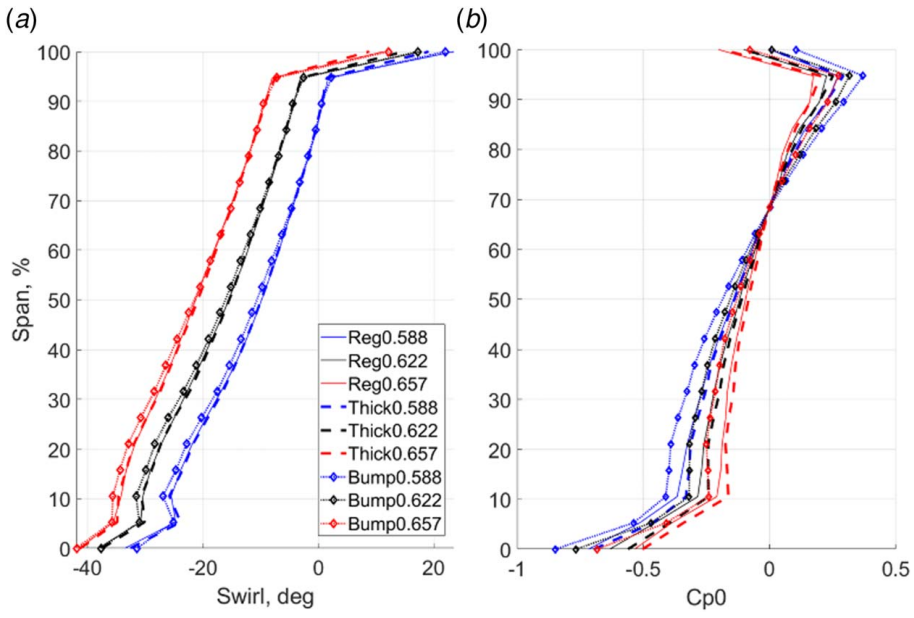

Fig. 12 (*a*) Circumferentially averaged inlet swirl angle and (*b*) total pressure coefficient for the regular, thick, and bump vanes at on- and off-design flow coefficients

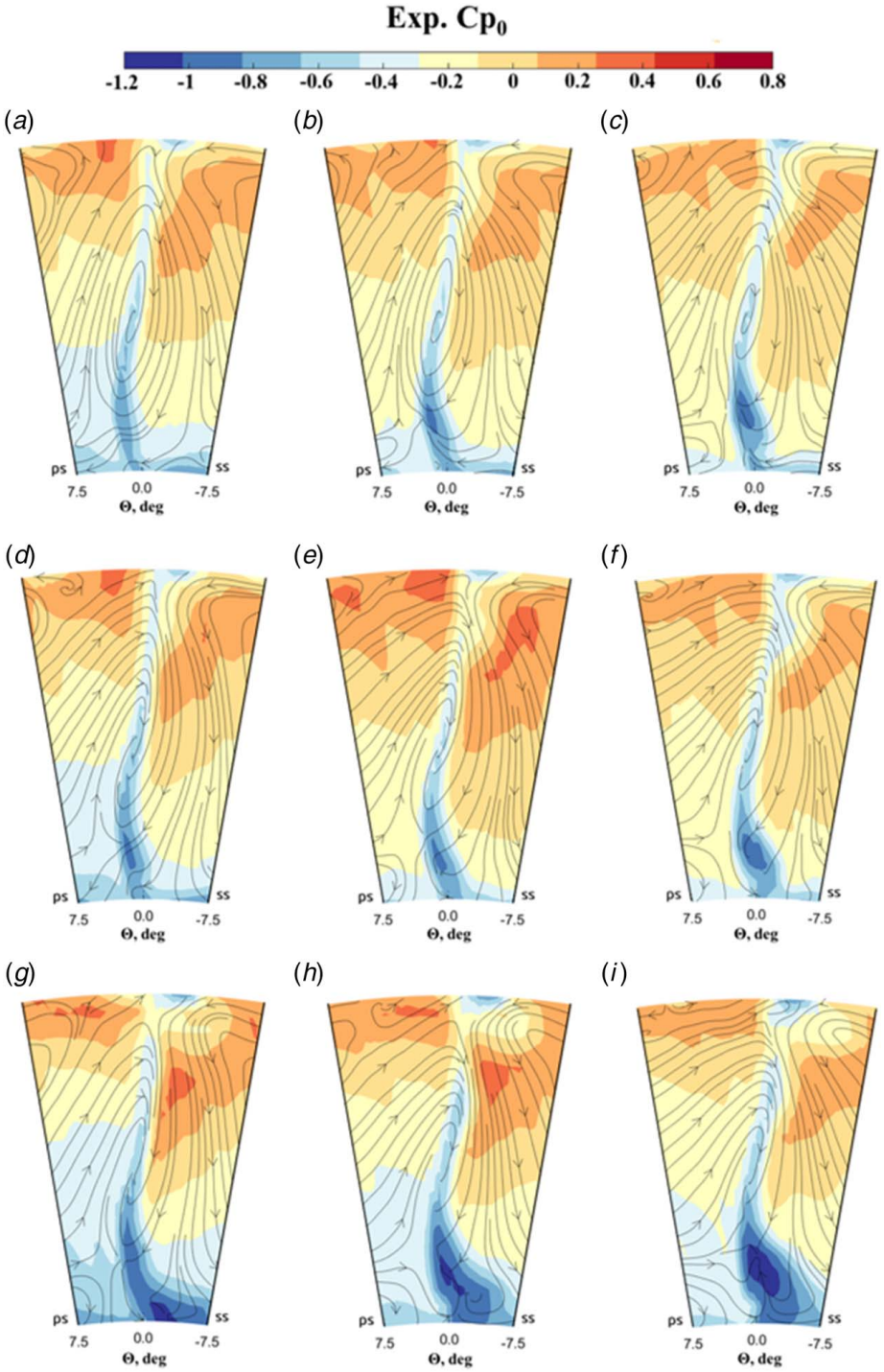

Fig. 13 Wake comparison for regular: (*a*) FC = 0.588, (*b*) FC = 0.622, and (*c*) FC = 0.657; thick: (*d*) FC = 0.588, (*e*) FC = 0.622, and (*f*) FC = 0.657; and bump: (*g*) FC = 0.588, (*h*) FC = 0.622, and (*i*) FC = 0.657 vanes at on- and off-design flow coefficients

More CFD details, covering also the thick vane and the bump sectors, will be published later in a more comprehensive validation study comparing the experimental results with numerical CFD predictions.

4 Summary and Conclusions

A detailed experimental aerodynamic study of an engine-realistic turbine rear structure is presented. The experiments were performed at low Mach numbers, but are nonetheless very relevant for engine conditions since in an aero-engine the flow is fully subsonic and there are no compressible effects in the TRS such as shocks or shock-boundary layer interactions.

For the first time, the investigated TRS configuration includes three types of OGVs typical for a modern state-of-the-art TRS: regular vanes, thickened vanes, and vanes with an engine-mount recess (a shroud bump). Each of the three OGV types was tested under on-design conditions and off-design conditions with a swirl angle varying ±5 deg from the aerodynamic design point.

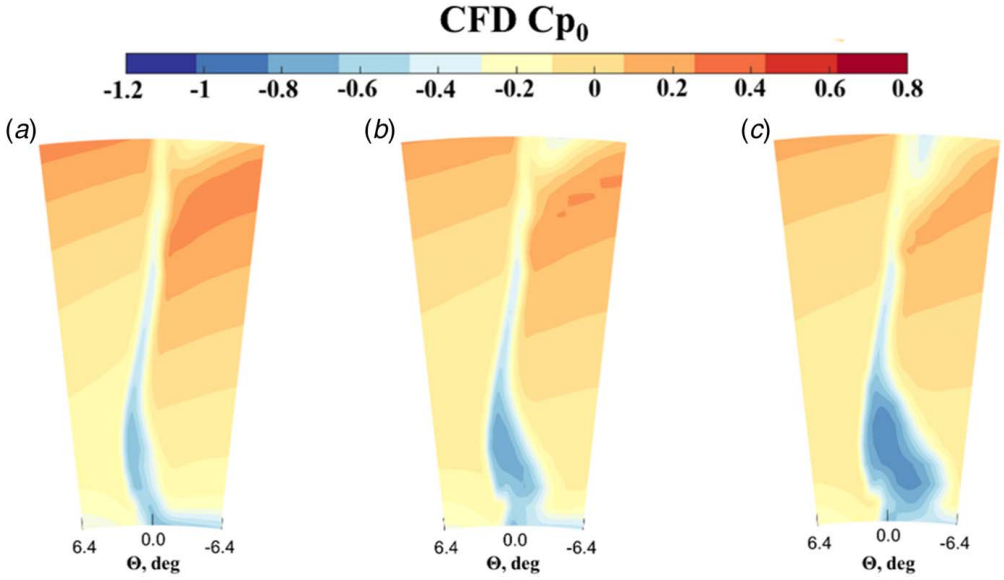

Fig. 14 CFD wakes for regular vane at on- and off-design flow coefficients: (*a*) FC = 0.588, (*b*) FC = 0.622, and (*c*) FC = 0.657

The flow out of the LPT stage into the TRS has a radial profile of total pressure and swirl angle. The inlet total pressure increases from the hub to the shroud. The absolute inlet swirl is higher close to the hub and is reduced down to almost axial flow at the shroud. Hence, the OGV loading is larger and the flow momentum is smaller near the hub than near the shroud. The largest pressure losses can be found in a region near the hub on the OGV suction side. The secondary flow from the hub-wall rolls up into a loss-core in the hub-suction side corner. Near the shroud, the situation is opposite and the local pressure losses are small. There is, however, a redistribution of the total pressure due to the secondary flow, which brings the high-momentum fluid from the hub to the bulk flow near the OGV suction side. It is not possible to model the presence of the above-mentioned radial flow non-uniformity in a linear cascade facility, which makes the current investigation particularly valuable.

As the flow coefficient increases, the absolute inlet swirl angle into the TRS increases, as does the OGV load. Increased flow coefficient results in a changed skewing of the inlet total pressure profile. As a result, the inlet swirl near the hub decreases and the OGV loading and the flow deceleration near the hub increase, resulting in increased total pressure losses. Local flow separation is created on the OGV suction side near the hub when the flow coefficient exceeds a certain limit. The flow separation results in a substantial local increase of the total pressure losses. The studied regular vane geometry is shown to handle the inlet swirl variation by ± 5 deg without any substantial loss increase in the near-hub region.

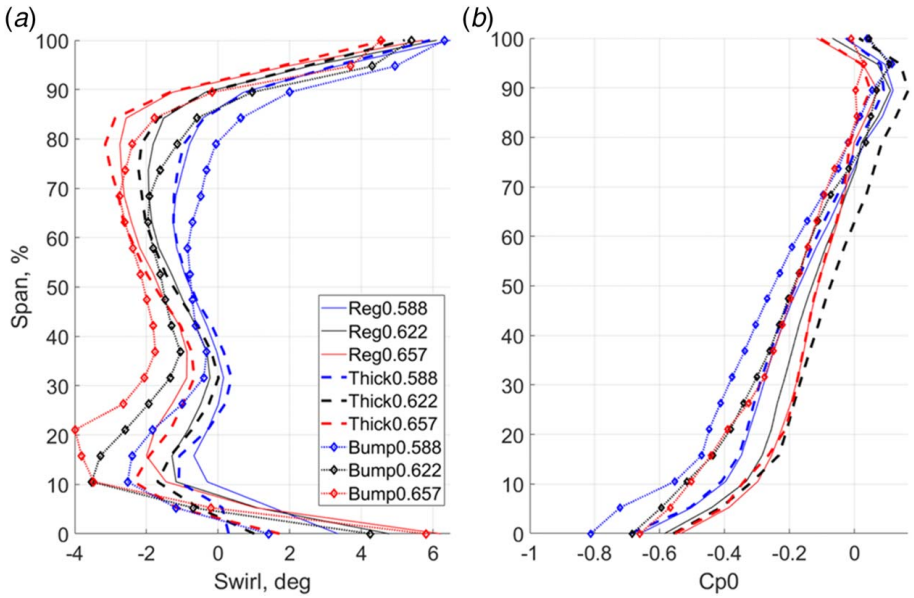

Fig. 15 (*a*) Circumferentially averaged outlet swirl angle (deg) and (*b*) total pressure coefficient (C_{p0}) for the regular, thick, and bump vanes at on- and off-design flow coefficients

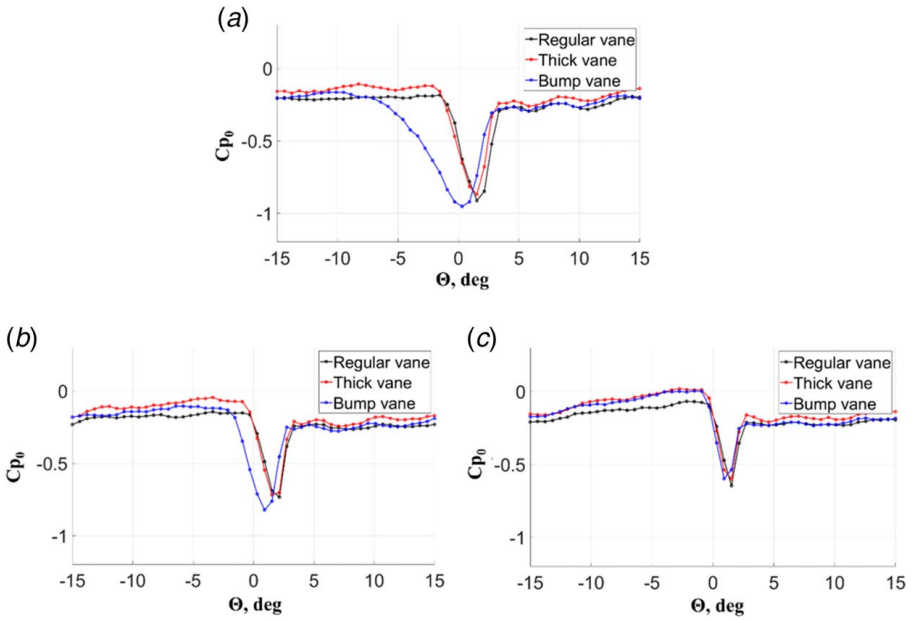

Fig. 16 Total pressure coefficient distributions for (*a*) 12, (*b*) 25, and (*c*) 32% spans for the regular, thick, and bump vanes at on-design flow coefficient

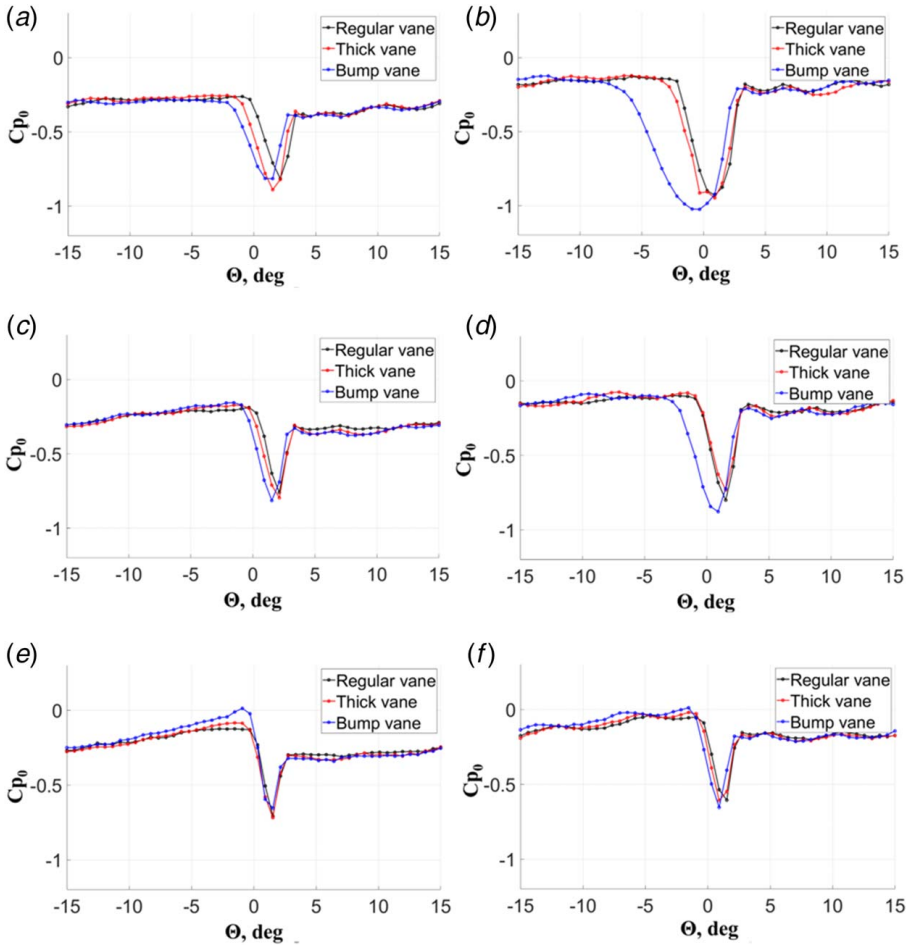

Fig. 17 Total pressure coefficient distributions for 12% span: (*a*) FC = 0.588 and (*b*) FC = 0.657; 25% span: (c) FC = 0.588 and (*d*) FC = 0.657; and 32% span: (*e*) FC = 0.588 and (*f*) FC = 0.657 spans for the regular, thick, and bump vanes at off-design flow coefficients

A thickened vane (so-called tube vane) is shown to have a similar aerodynamic performance as the regular vane. The increased vane thickness results in increased blockage and an increased suction-side diffusion and changed skewing of the inlet total pressure profile without affecting the inlet swirl profile. However, despite the substantially increased OGV load on the thickened OGV and increased flow deceleration on the OGV suction side, the thickened OGV is shown to handle the on-design and off-design conditions without a substantial increase of the total pressure loss and without loss of the turning performance. The oil-flow visualization at flow coefficient 0.657 has revealed a small flow separation on the OGV suction side near the hub and a small laminar separation bubble with reattachment near the suction-side peak; however, these two flow separations were observed on a regular vane as well. A minor loss increase near the hub is observed, and the vane profile loss (a 2D loss at mid-span) did not change as compared to the regular vane, which showed a good vane design. It can be noted, however, that the thickened vane can potentially have an upstream influence on the LPT by locally affecting the upstream static pressure.

An engine-mount recess (a shroud bump) is shown to affect the OGV aerodynamics more substantially. A shroud bump is structural enforcement of the TRS shroud, which protrudes into the TRS gas path. The bump is shown to have a strong local effect on the OGV wall pressure distribution near the shroud which gradually decreases toward the hub. The current bump design did not reveal any flow separation on the bump itself under on- and off-design conditions. However, the bump is found to affect the OGV aerodynamics indirectly by influencing the inlet conditions into the TRS (the total pressure and swirl profiles) and by increasing the losses in the near-hub region of the OGV. The profile loss at the OGV mid-span is not affected, while a substantial loss increase near the hub (more than double) under on- and off-design conditions is observed. It is notable that the bump influences the OGV losses not only due to the change of the OGV static; the upstream influence on the inlet conditions plays an important role as well. For the vanes under the current study, the bump effect on the OGV static pressure in the hub region is less than the effect from the vane thickening, though the losses for the bump are larger. The upstream influence of the bump on the LPT outlet conditions leads to an absolute swirl increase by approximately 1 deg and to a changed radial gradient of the total pressure profile. The influence of the bump on the TRS outlet flow, apart from the increased losses, leads to a notable flow overturning in the shroud region and underturning in the hub region, where separation occurs.

Acknowledgment

The authors would like to thank Isak Jonsson for the regular vane data presented in this work and for supporting current experiments. Chalmers Laboratory of Fluids and Thermal Sciences is acknowledged for hosting the facility and the measurement equipment.

Funding Data

- Nationella flygtekniska forskningsprogrammet (NFFP) Clean Sky 2 Joint Undertaking under the European Union's Horizon 2020 Research and Innovation Program (Grant No. 821398).

Conflict of Interest

There are no conflicts of interest.

Data Availability Statement

The data sets generated and supporting the findings of this article are obtainable from the corresponding author upon reasonable request. Data provided by a third party are listed in Acknowledgment.

Nomenclature

ν = kinematic viscosity, m^2/s
x = streamwise coordinate, m
FC = flow coefficient, U_x/V
H = channel height at inlet, m
V = blade velocity, m/s
C_p = static pressure coefficient, $(P_s - P_{sref})/(P_{tref} - P_{sref})$
C_{p0} = total pressure coefficient, $(P_t - P_{tref})/(P_{tref} - P_{sref})$
P_s = static pressure, Pa
P_t = total pressure, Pa
U_x = axial flow velocity, m/s
Re = Reynolds number, $U_x H/\nu$
Θ = angular coordinate, deg

References

[1] Hjärne, J., Larsson, J., and Löfdahl, L., 2006, "Performance and Off-Design Characteristics for Low Pressure Turbine Outlet Guide Vanes: Measurements and Calculations," Proceedings of the ASME Turbo Expo 2006, Paper No. GT2006-90550.
[2] Hjärne, J., Larsson, J., and Löfdahl, L., 2003, "Design of a Modern Test Facility for LPT/OGV Flows," Proceedings of the ASME Turbo Expo 2003, Paper No. GT2003-38083.
[3] Hjärne, J., Chernoray, V., Larsson, J., and Löfdahl, L., 2005, "Experimental Evaluation of the Flow Field in a State-of-the-Art Linear Cascade With Boundary Layer Suction," Proceedings of the ASME Turbo Expo 2005, Paper No. GT2005-68399.
[4] Hjärne, J., Chernoray, V., Larsson, J., and Löfdahl, L., 2006, "An Experimental Investigation of Secondary Flows and Loss Development Downstream of a Highly Loaded Low Pressure Turbine Outlet Guide Vane Cascade," Proceedings of the ASME Turbo Expo 2006, Paper No. GT2006-90561.
[5] Hjärne, J., Chernoray, V., Larsson, J., and Löfdahl, L., 2007, "Numerical Validations of Secondary Flows and Loss Development Downstream of a Highly Loaded Low Pressure Turbine Outlet Guide Vane Cascade," Proceedings of the ASME Turbo Expo 2007, Paper No. GT2007-27712.
[6] Selic, T., Lengani, D., Marn, A., and Heitmeir, F., 2012, "Aerodynamic Effects of an Unshrouded Low Pressure Turbine on a Low Aspect Ratio Exit Guide Vane," Proceedings of ASME Turbo Expo 2012, Paper No. GT2012-68981.
[7] Rojo, B., Kristmundsson, D., Chernoray, V., Arroyo, C., and Larsson, J., 2015, "Facility for Investigating the Flow in a Low Pressure Turbine Exit Structure," Proceedings of the 11th European Conference on Turbomachinery Fluid Dynamics and Thermodynamics, ETC 2015, Madrid, Spain, Mar. 23–27, Paper No. ETC2015-235, pp. 1–13.
[8] Jonsson, I., Chernoray, V., and Dhanasegaran, R., 2019, "Infrared Thermography Investigation of Heat Transfer on Outlet Guide Vanes in an Engine Exit Module," Proceedings of the 13th European Turbomachinery Conference on Turbomachinery Fluid Dynamics and Thermodynamics, ETC 2019, Lausanne, Switzerland, Apr. 8–12, Paper No. ETC2019-243, pp. 1–13.
[9] Jonsson, I., Chernoray, V., and Rojo, B., 2018, "Surface Roughness Impact on Secondary Flow and Losses in a Turbine Exhaust Casing," Proceedings of the ASME Turbo Expo 2018, Paper No. GT2018- 75541.
[10] Jonsson, I., Deshpande, S., Chernoray, V., Thulin, O., and Larsson, J., 2020, "Experimental and Numerical Study of Laminar-Turbulent Transition on a Low-Pressure Turbine Outlet Guide Vane," Proceedings of the ASME Turbo Expo 2020, Paper No. GT2020-1787.
[11] Hjärne, J., Chernoray, V., and Larsson, J., 2008, "Experimental Investigations and Numerical Validation of an Outlet Guide Vane With an Engine Mount Recess," Proceedings of the ASME Turbo Expo 2008, Paper No. GT2008-50168.
[12] Arroyo, C., 2009, "Aerothermal Investigation of an Intermediate Turbine Duct," Ph.D. dissertation, Chalmers University of Technology, Gothenburg, Sweden.
[13] Hjärne, J., 2007, "Turbine Outlet Guide Vane Flows," Ph.D. dissertation, Chalmers University of Technology, Gothenburg, Sweden.
[14] Menter, F. R., Langtry, R. B., Likki, S. R., Suzen, Y. B., Huang, P. G., and Völker, S., 2006, "A Correlation-Based Transition Model Using Local Variables—Part I: Model Formulation," ASME J. Turbomach., **128**(3), pp. 413–422.

Paper 2

Valentin Vikhorev, Valery Chernoray. **Experimental Flow Analysis in a Modern Turbine Rear Structure with 3D Polygonal Shroud Under Realistic Flow Conditions,** Proceedings of 14th European Conference on Turbomachinery Fluid dynamics and Thermodynamics, 2021, ETC2021-539.

EXPERIMENTAL FLOW ANALYSIS IN A MODERN TURBINE REAR STRUCTURE WITH 3D POLYGONAL SHROUD UNDER REALISTIC FLOW CONDITIONS

V. Vikhorev, V. Chernoray

Chalmers University of Technology, Gothenburg, Sweden
valvik@chalmers.se, valery.chernoray@chalmers.se

ABSTRACT

Continuous advancement of the existing design of turbine rear structure (TRS) leads to new challenges in terms of aerodynamic efficiency. This work presents experimental aero studies of the effect of the 3D polygonal shroud in the TRS comprising several types of guide vanes representative of a modern TRS: regular vanes, thickened vanes, and vanes with a mount bump. The experiments were performed in an engine-realistic facility for a fixed Reynolds number, 350000, and three operation points based on a low-pressure turbine (LPT) exit swirl angle. The current study shows that the thickened vane handles the on-design and off-design conditions with good aerodynamic performance. It is observed that a shroud bump significantly affects the pressure losses because of the additional vorticity region created from the bump itself, and it has an upstream influence on the outlet flow from the LPT.

KEYWORDS

TURBINE REAR STRUCTURE, TURBINE EXHAUST CASING, LOW-PRESSURE TURBINE, OUTLET GUIDE VANE, OUTLET MOUNT RECESS

NOMENCLATURE

C_{p0}	*total pressure coefficient,* $(P_t–P_{t,ref})/(P_{t,ref}–P_{s,ref})$
C_p	*static pressure coefficient,* $(P_s–P_{s,ref})/(P_{t,ref}–P_{s,ref})$
FC	*flow coefficient, Ux/V*
H	*channel height at inlet, m*
PS	*pressure side*
P_s	*static pressure, Pa*
P_t	*total pressure, Pa*
Re	*Reynolds number,* U_xH/v
SS	*suction side*
V	*blade velocity, m/s*
U_x	*axial flow velocity, m/s*
x	*streamwise coordinate, m*
v	*kinematic viscosity,* m^2/s
Θ	*angular coordinate, deg*

INTRODUCTION

One of the main challenges of current air transport systems is aimed at achieving resource-efficient, climate- and environmental-friendly level. In compliance with this requirement, including the global environmental targets such as reduction of fuel consumption, carbon dioxide emissions and relative to the engine noise, modern geared turbofan engines are being developed.

Enabling the fan and turbine to rotate at different speeds provided by geared turbofan engines significantly increases the by-pass ratio and, therefore, the propulsive efficiency. At the same time the swirl angles from the last low-pressure turbine (LPT) rotor to the turbine rear structure (TRS) can be kept lower. However, with geared engines the off-design variations of the outlet swirl angle increases,

which makes it more aerodynamically challenging to design TRS with built-in outlet guide vanes (OGV) to recover the swirl flow and increase the thrust for all operating points of the turbine.

In addition, modern turbofan engines must satisfy all structural and engineering requirements of the engine. Therefore, state-of-the-art TRS often requires a three-dimensional polygonal shape and comprises several vane types: regular vanes, thickened vanes with additional space for bearing oil pipelines, and vanes with mount bumps for attachment to the engine. From the perspective of aerodynamics, such engine-relevant modifications for shroud geometry as well as vane geometry can affect the development of end-wall boundary layers or even triggers possible flow separations, thereby, increasing pressure losses. Therefore, TRS development is directly related to the need for its aerodynamic investigation.

Because of the lower cost and easier implementation, the annular arrangement of a TRS blade row is often simplified by a linear arrangement. Therefore, the first experimental investigations of the secondary flow development were carried out by Hjärne et al. (2006) in a linear cascade, providing insight into the interaction of boundary layers coming from OGV, hub and shroud in TRS. In further work by Hjärne et al. (2007), numerical validation of secondary flow evolution was performed. In addition, to deepen the analysis for the turbulence models, the authors also considered the effect of secondary flows on the downstream losses. Sonoda et al. (2008) compared two alternatively designed cascades and provided new insight on the flow mechanisms around the end-wall region. However, two-dimensional approximation of vanes suffers from weaknesses such as lack of possibility to simulate radial pressure gradients and limited flow periodicity.

Regarding the problems mentioned above, the annular cascade reproduces the flow conditions more realistically than a linear cascade. Selic et al. (2012) were the first to investigate the effect of the leakage flow on the flow structure of the OGV in an annular rig with an unshrouded turbine. Radial variation in swirl, total pressure and yaw angle over the passage height as well as three-dimensional effects were investigated by Schönleiner et al. (2014). Further works were done in an engine-realistic facility with shrouded LPT located at the Chalmers University of Technology. Considerable efforts were made by Jonsson et al. (2019) to measure heat transfer on regular OGVs for several design conditions indicating the laminar-turbulent transition, which is crucial for the TRS performance. More detailed investigation of regular OGV's with additional CFD results can be found in a recent paper written by Jonsson et al. (2020).

Besides, as mentioned above, modern TRS includes several vane types. Therefore, it is crucial to consider the aerodynamic performance of each type of vane and their mutual influence. The influence of the vane with mount bump in the linear cascade was previously studied by Hjärne et al. (2008). In addition, Vikhorev et al. (2020) also carried out aerodynamic studies. They revealed a significant effect of the bump vane on pressure losses in the near-hub region of the OGV and upstream influence on the inlet conditions.

Moreover, the authors performed an oil-film visualization to demonstrate the flow behaviour around OGV's and compared the patterns for the different design conditions. These measurements were done in an annular engine-realistic rig with a circular shroud. However, aerodynamic investigations for the TRS with polygonal shroud geometry have not previously been conducted. Therefore, the main goal of this work is to study the effect of a 3D polygonal shroud design in a modern TRS including several vane types: regular vanes, vanes equipped with bump and vanes with increased thickness to give more internal space for the passage of the bearing oil pipes and scavenge tubes. The engine realistic TRS with all three vane types mounted simultaneously was investigated to consider the mutual influence between the vanes.

EXPERIMENTAL FACILITY AND INSTRUMENTATION

The experimental study of the engine-realistic TRS was conducted in an annular low-speed large-scale 1.5 stage LPT-OGV facility at Chalmers University of Technology, Sweden. The schematic view of the facility is shown in Fig. 1. The airflow driven by a 250-kW centrifugal fan passes through corner ducts and diffusers. After the expansion, the flow enters the settling chamber with stainless

steel screens and honeycomb to remove non-uniformities of the flow. Following this, the flow passes through the contraction and reaches an LPT stage which is required to simulate realistic boundary conditions to the TRS. The LPT stage comprised stator stage with 60 nozzle guide vanes (NGVs) and rotor stage with 72 blades and was designed by GNK Aerospace Engine Systems, Sweden.

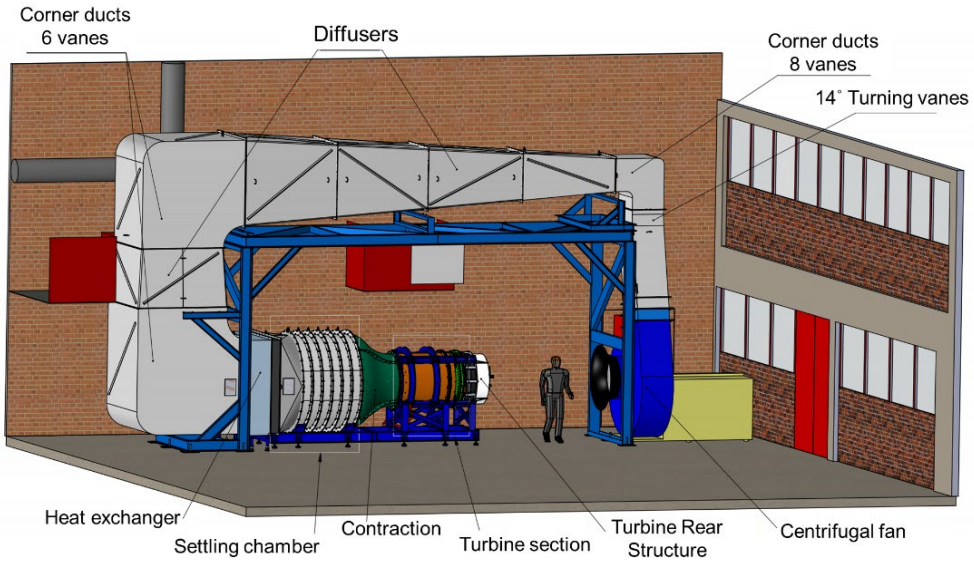

Figure 1: 3D view of the high-Reynolds number continuous operation LPT-OGV facility

The Reynolds number in a TRS of an aero-engine based on channel height and axial velocity ranges from 100000 to 600000 depending on the engine type and size. The flow coefficient (FC), is a second main parameter of the facility, determining the turbine load, and defined as the ratio of the axial velocity to the blade speed:

$$\boldsymbol{FC = U_x/V} \tag{1}$$

The TRS section of the facility is built to be modified and, for the current configuration, designed by GKN Aerospace Engine Systems. It comprises 12 OGVs with a 3D polygonal shroud design (Fig. 2a). It shall be noted that the LPT and TRS components have been designed solely for the experimental rig and are not related to any GKN Aerospace product characteristics.

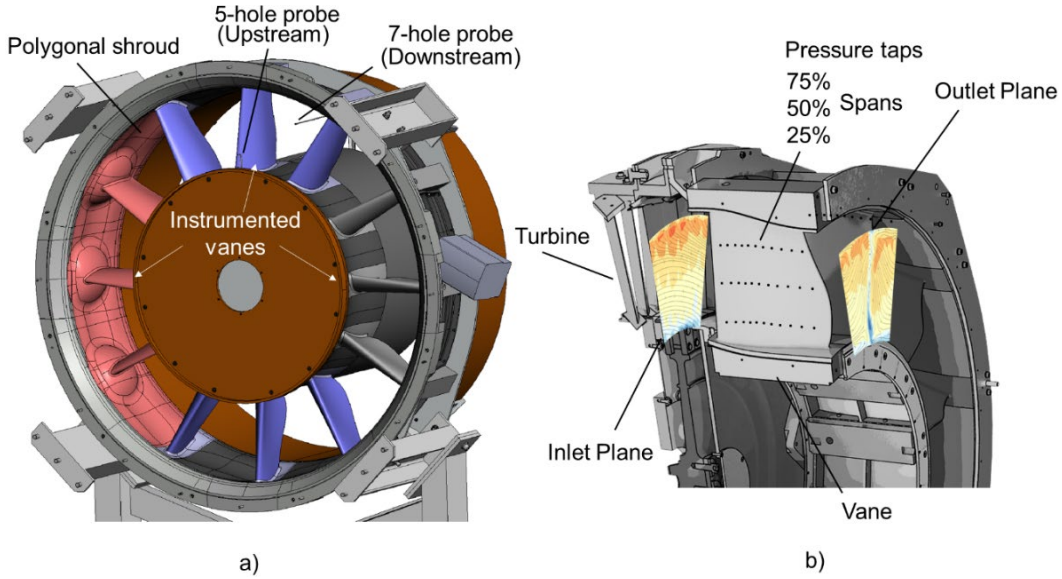

Figure 2: 3D model of tested Turbine Rear Structure

There are two internal traversing systems installed in the TRS section needed to position probes. Both systems are working independently and capable of moving in radial and circumferential directions. Moreover, one traversing system is equipped with an additional motor enabling the downstream probe to be positioned in the axial direction, and therefore, the traversing systems cover near full-volume of the TRS section. The positioning and data acquisition is controlled by a PC with in-house LabVIEW® (National Instruments Corporation, Austin, TX, USA) software scripts. The accuracy of positioning in the circumferential directions is 0.01° while in the radial and axial directions are 0.075 mm.

The total pressure and swirl measurements are accomplished using pre-calibrated 5-hole and 7-hole aero probes, located upstream (Inlet plane) and downstream (Outlet plane) respectively (Fig. 2b). Wall pressure measurements on the vane and shroud bump were done using two Scanivalve mechanical multiplexers with 48 ports each. Acquisition of pressure data was performed using a 16-channel PSI-9116 system with a 500 Hz sampling rate and 2.5 seconds of sampling time. This data was time averaged and only average values were analysed. Pressure values were acquired relative to the total pressure taken from a stationary Prandtl tube located in the bulk flow region between OGVs at 0.7 chord distance from the leading edge.

Furthermore, obtained pressure data were processed and converted to the form of non-dimensional coefficients (Eq. 2 and 3).

$$C_{p0} = \frac{P_t - P_{t,ref}}{P_{t,ref} - P_{s,ref}} \tag{2}$$

$$C_p = \frac{P_s - P_{s,ref}}{P_{t,ref} - P_{s,ref}} \tag{3}$$

Tests are performed at on-design and off-design conditions. The flow Reynolds number of 350000 is used for all three operation points. The flow coefficient values and, respectively, averaged LPT exit swirl angles (the TRS inlet conditions) are summarized in Table 1, where on-design parameters are marked with green.

	Off-design (low loading)	**On-design**	Off-design (high loading)
Flow coefficient	0.555	0.622	0.66
Inlet swirl angle	-6.3	-16.9	-22.4
Reynolds number	350000		

Table 1: TRS inlet conditions

Following the goal of weight reduction, the current configuration consists of 6 thin vanes, called regular vanes. However, the requirement of allowing oil pipelines to pass through OGVs leads to the enlarged thickness of the OGVs. In addition, recent TRS designs require integration of vanes with sunken engine-mount bumps. Therefore, the test section was equipped with three thick vanes and three bump vanes together with six regular vanes.

Figure 3 shows the 3D models of regular, thick and bump OGVs, which were manufactured with SLA rapid prototyping technology. Compared to the regular OGV, the mid-span airfoil section of the thick OGV has an increased thickness by 45% while the camber line was designed the same. The vane surfaces were fitted with pressure taps to measure static pressure distribution and obtain aerodynamic loads. For three spans (25, 50 and 75%) the pressure taps covered pressure and suction sides. For the bump vane, the bump was equipped with extra pressure taps on its surface.

Oil-film visualizations were carried out for the thick and bump vane due to the expected different nature of the flow development. The visualizations were performed using the oil-film technique at different design conditions. A mixture of a mineral oil and TiO2 powder, with particles from 0.2 to 0.3 µm was used. The flow patterns were captured using a digital camera GoPro Hero4.

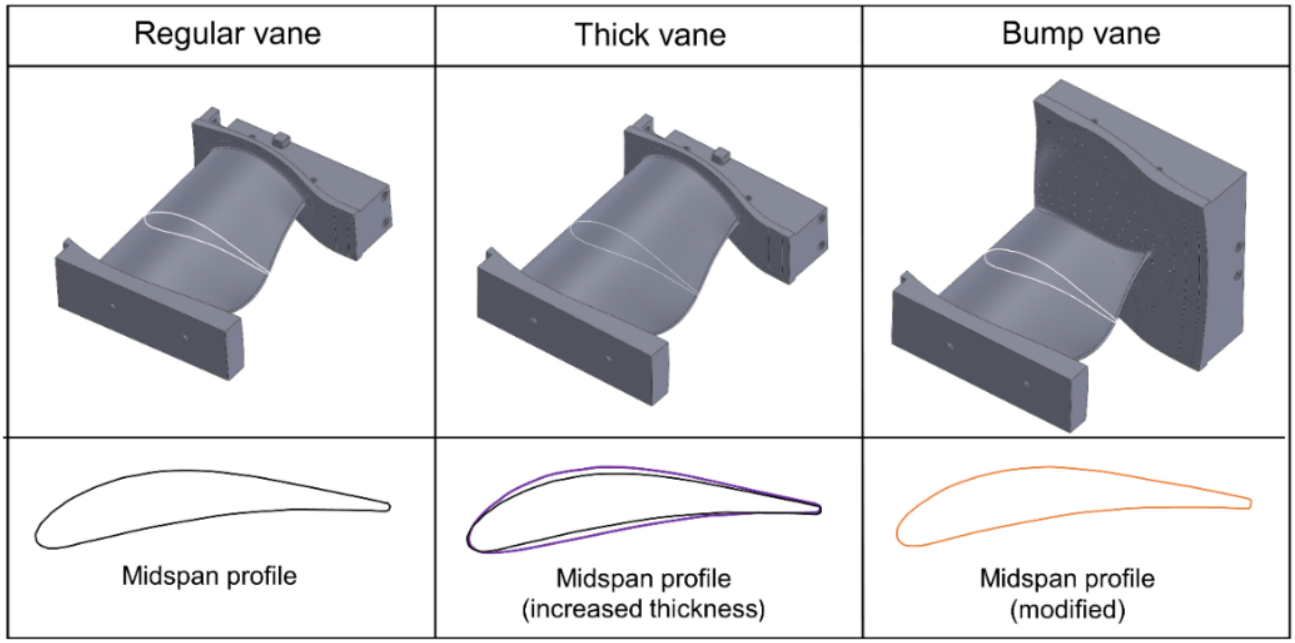

Figure 3: 3D models of regular, thick and bump vanes with their midspan profiles

RESULTS AND DISCUSSION

This section presents the results and discussions concerning the experimental investigations divided into two sections according to the type of measurements. The following results were obtained for the new configuration, including 3D polygonal shroud and three types of vanes: regular, thick and bump vanes.

Pressure measurements

Inlet and outlet measurements

Inlet measurements were performed for a 30-degree sector located upstream of the OGV. The azimuthal resolution was 0.6˚ and radial resolution was 9.7 mm. Figure 4 shows the comparison of upstream total pressure distributions for the regular, thick and bump vane at on-design condition.

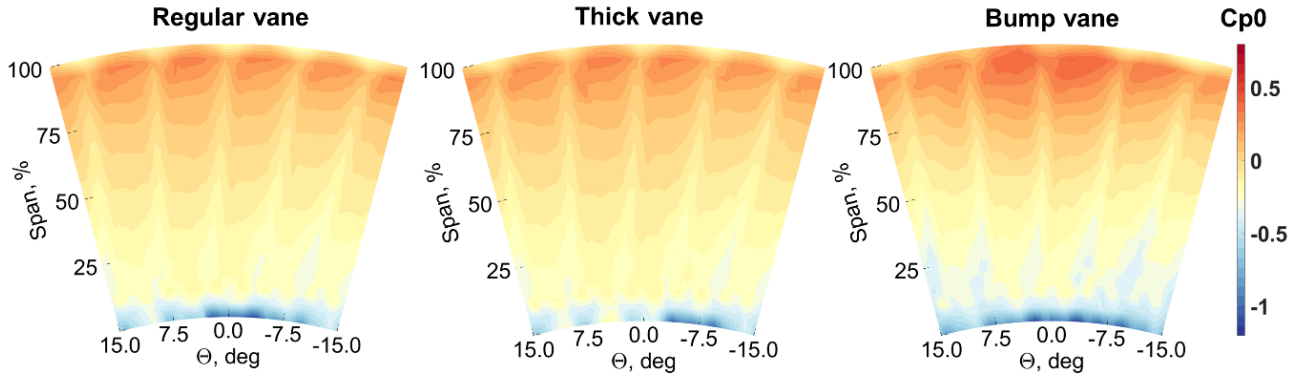

Figure 4: Inlet total pressure coefficient distributions for regular, thick, and bump vanes at on-design condition

Concerning the flow structures coming from the LPT stage, stator wakes developed from NGVs can be observed for all configurations. In addition, the presence of vortex pair developed from each NGV's results in local pressure drop near the hub region. A more detailed explanation of the flow development upstream of the TRS section can be found in Arroyo, 2009 and Rojo, 2015.

Circumferentially averaged profiles of swirl angle and total pressure coefficient are presented in Fig.5. The figure shows that the upstream influence of the thickened vane is quite similar compared to the regular vane, although the vane has enlarged thickness. However, for the vane with a mount-recess the bump results in redistribution of the upstream circumferentially averaged total pressure, which also causes a swirl reduction in the shroud region. The blockage of the flow due to the bump implementation leads to the pressure redistribution and therefore changes the inflow pressure conditions upstream of the OGV. The bump leads to a more skewed inlet total pressure profile shown by a red plot in the right figure.

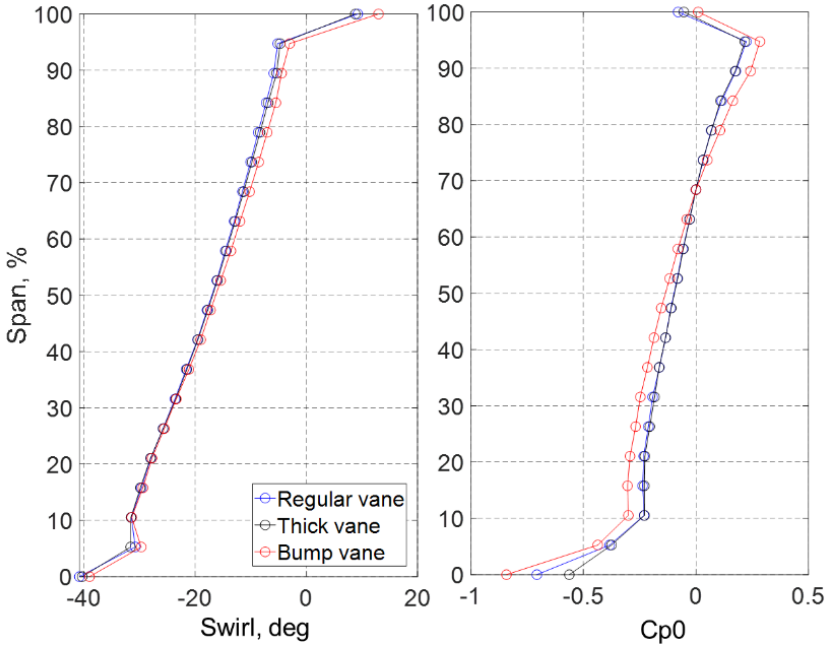

Figure 5: Circumferentially averaged inlet profiles for regular, thick and bump vanes at on-design condition.

Outlet measurements were performed for a 30-degree sector located downstream of the OGV. The circumferential resolution was 0.6˚ and radial resolution was 9.7 mm. The focus of this part of the study is on the wake comparison at on- and off-design conditions. For that reason, normalized pressure data are presented for a cropped 15-degree sector, which contains the downstream wake (Fig.6).

The secondary flow developed in the hub suction side corner is the main source of pressure losses. Therefore, the hub region is the most sensitive to the additional pressure losses. For the regular and thick vane, the wake intensity changes only for the high loading condition, which can be explained by a formation of a small separation bubble near the vane trailing edge close to the hub, which is shown by the flow visualizations in the next section of the paper. However, for the low loading case and on-design condition, there is no noticeable difference in the wake formation between regular and thick vanes.

For the bump vane, the influence of the bump is significant. It results in extra pressure losses located near the shroud, which can be seen for the on- and off-design conditions. The nature of the wake formation in the shroud region for the bump vane is different because of the interaction of the boundary layers coming from the bump as well as from the OGV. Even for the low loading case, this region with extra losses should be taken into account.

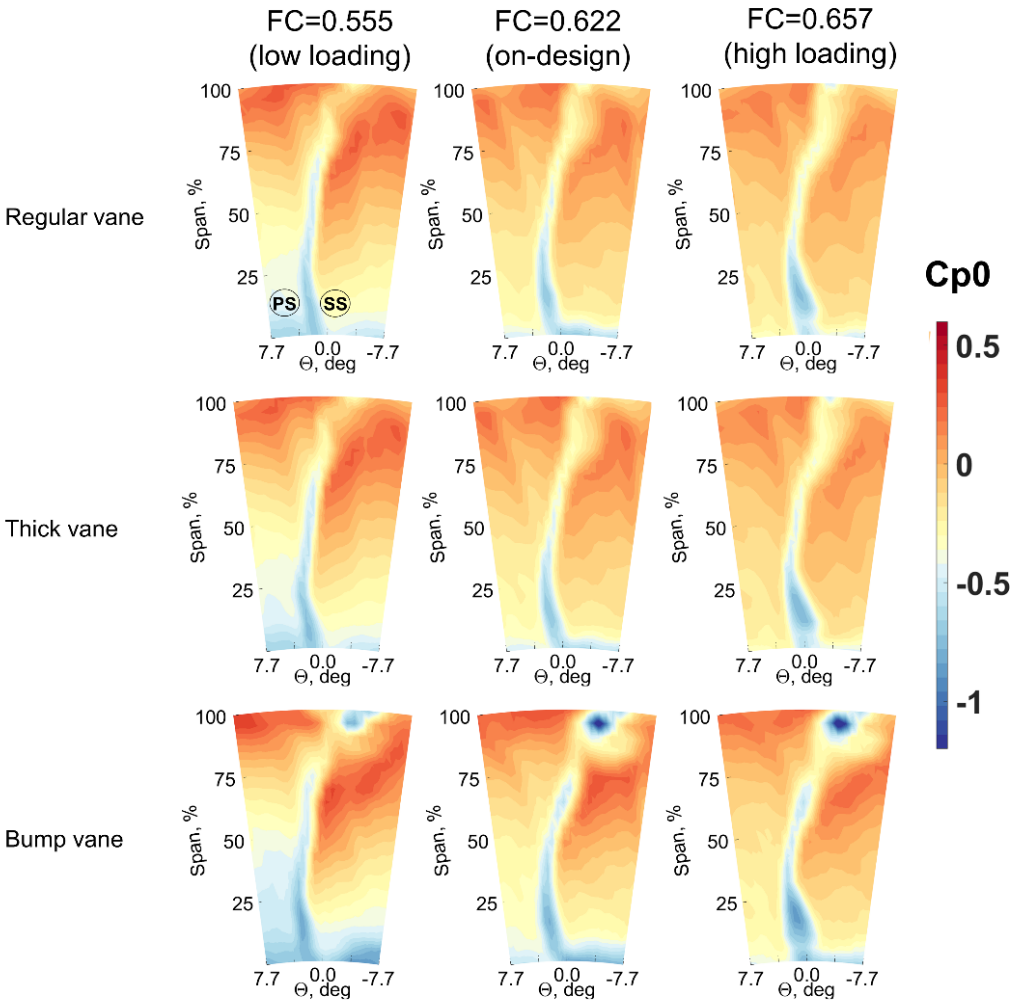

Figure 6: Outlet total pressure coefficient distributions for regular, thick and bump vanes at on- and off-design conditions

Figure 7 presents vorticity distributions at on-design conditions. Streamlines of the flow plotted using crossflow velocity components are also added to these profiles. Apart from the region of a decelerated fluid with higher vorticity values for all vanes, one can observe a well-pronounced region of the increased vorticity for the bump vane. The boundary layer developed from the bump surface has separated from the rear of the bump, as will be shown by the flow visualizations. Therefore, a strong vorticity region with decelerated fluid has been created. As can be seen, vorticity values in the core of this vortical structure are twice higher than the values in the wake region.

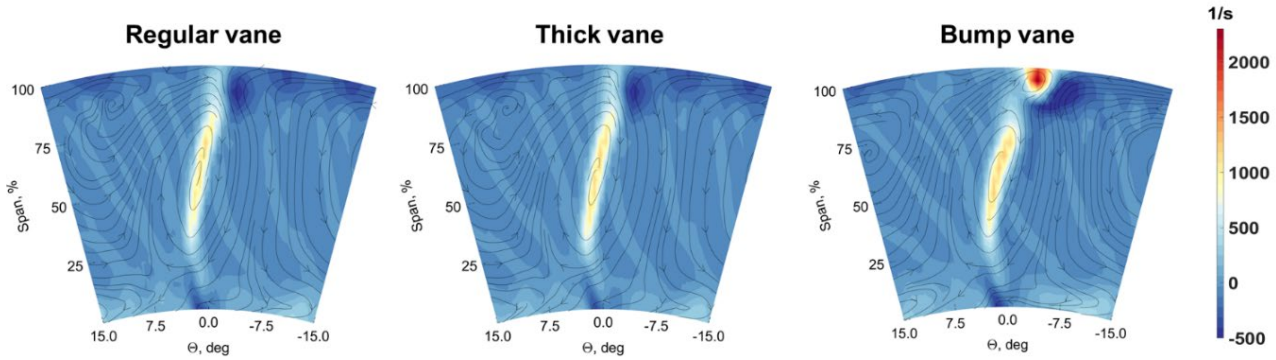

Figure 7: Downstream vorticity distributions for regular, thick and bump vanes at on-design condition

Static pressure measurements

This section presents results of the vane pressure measurements performed for regular, thick and bump vanes as well as pressure measurements on the bump surface.

The distribution of the static pressure coefficient at on-design condition is shown in Fig 8.

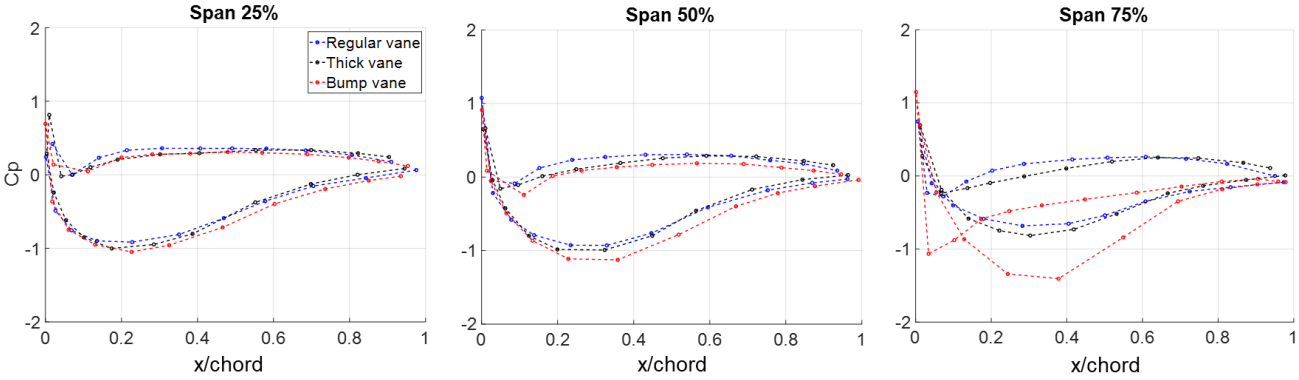

Figure 8: Static pressure distributions for regular, thick and bump vanes at on-design condition

Comparative analysis of these profiles shows that thickening of the vane, as well as presence of bump vane, creates a blockage for the passing flow. Therefore, it leads to a decrease in static pressure for the modified vanes. However, for the bump vane, the static pressure is very significantly affected at 75% span, which can be explained by the strong local influence of the bump. The flow acceleration near the front part of the bump results in much lower static pressure values both for the pressure and suction side, while the suction peak shifts downstream. Downstream flow expansion after a physical bump peak point leads to the flow deceleration. Consequently, the streamwise pressure gradient is significantly higher for the red curve from 40% chord to 70% chord.

Figure 9 presents normalized static pressure on the bump surface for different inflow conditions. For the lowest flow coefficient and, correspondingly, low loading case, a region with the lowest static pressure is located on the pressure side. For the on-design case, one can compare the previously shown profiles for the vane at 75% and the pressure distribution on the bump. As seen, the pressure minimum on the bump suction side is consistent with suction peak for the previous static pressure distribution. For the high loading case, the static pressure on the bump decreases on the vane suction side and increases on the vane pressure side. Therefore, there is a clear interaction of pressure distribution on the bump with pressure distribution on the OGV.

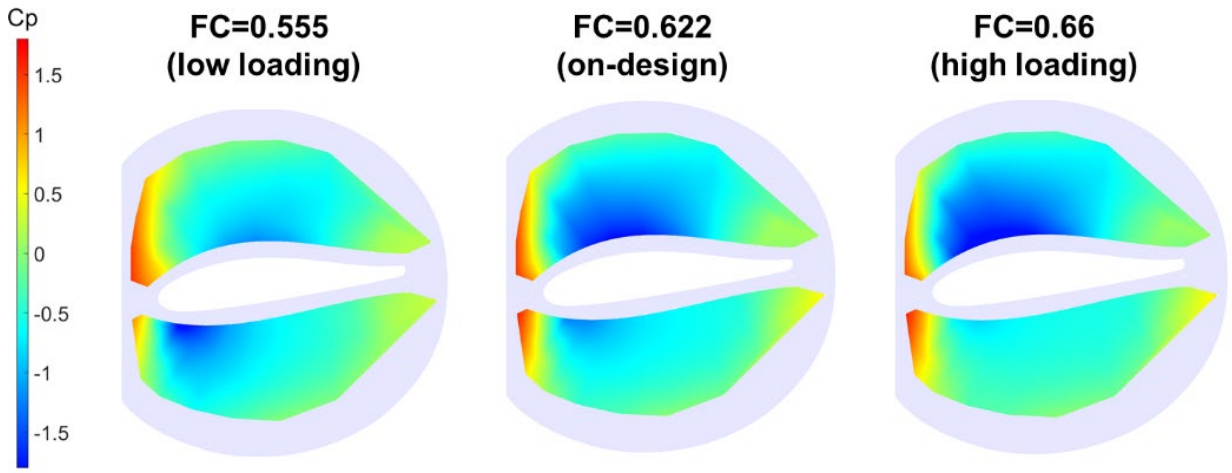

Figure 9: Static pressure distributions on the bump at on- and off-design conditions

Flow visualizations

The oil-film technique is an efficient qualitative tool in highlighting near-wall streamlines and flow separation regions. The focus of this section is on oil-film visualizations performed for thick and bump OGVs. Streamlines showing the flow development near the wall were obtained from the dynamic analysis of the flow visualization sequences and added to the visualization pictures. The results shown here are for the vane suction side at different flow coefficients. The suction side is the most influenced by the vane geometry and inlet conditions.

The flow visualizations for the thick vane are shown in Fig.10. At the off-design point with low loading, there are no flow separations, and streamlines are slightly distorted near the suction side peak due to the interplay of the radial and streamwise pressure gradients. There is also a clear streamline deviation near the hub due to the flow diffusion in the corner.

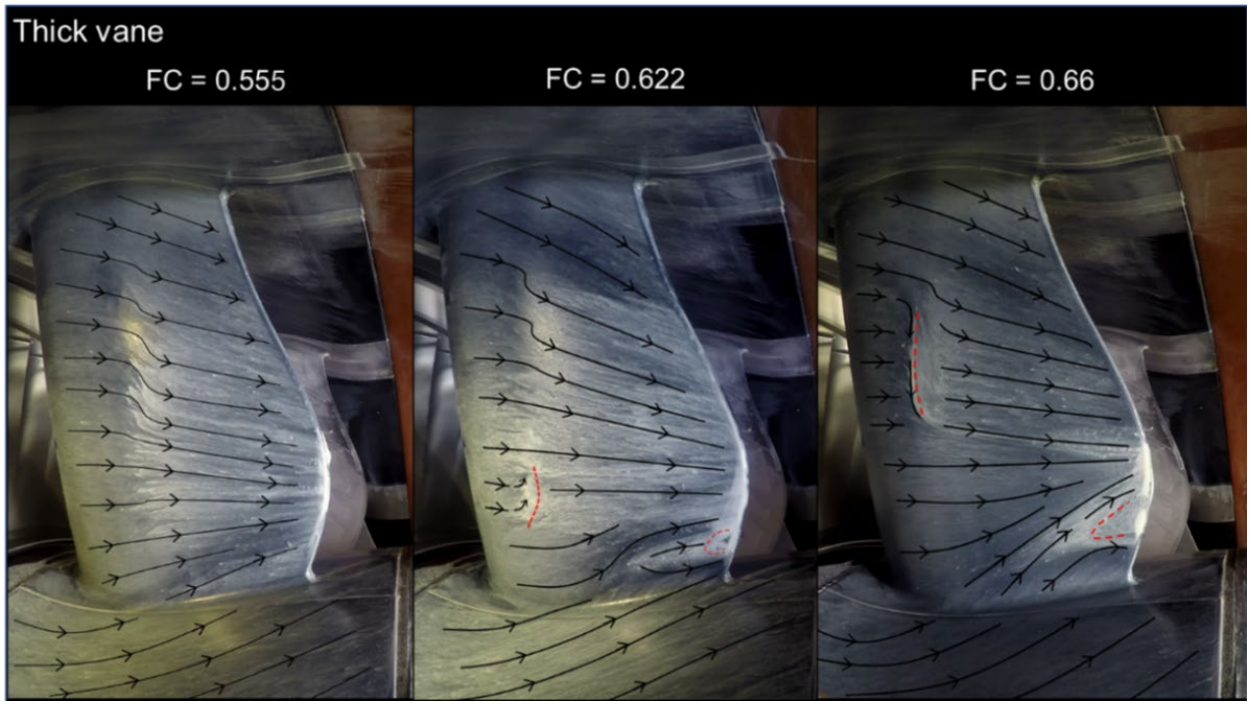

Figure 10: Oil-film visualizations for the thick vane at on- and off-design conditions

Moreover, based on visualizations on the pressure side, which are not provided here, and static pressure contours for the bump, the stagnation line is located near the leading edge without indication of any flow separations on the OGV pressure side. Increasing the load, two deceleration zones, marked with red dashed lines, are being formed. A small region located at approximately 15-20% axial chord and 25% span with concentrated powder particles reflects the presence of the flow stagnation, which can be a small separation bubble with further reattachment. In addition to this region, a small stagnation area is formed near the hub and vane trailing edge which can be explained as highly diffused interaction of the boundary layers coming from the OGV and the hub. Even for the high loading case, this region does not indicate reversed flow, while the area with accumulating particles grows and shifts towards the mid-span.

In contrast to the flow on the thick vane, for the bump vane, the flow has some pronounced differences (Fig. 11). For the on-design condition, the visualization does not indicate a clear flow stagnation in the hub corner near the vane trailing edge. However, there is a stagnation region with accumulated particles located at 20-25% of axial chord and 25% span. The location of this deceleration zone (0.45% chord) is consistent with the location of the suction peak from wall-pressure measurements. For the high loading case, this region is shifted towards the shroud as for the thick vane. As well a region with flow reversal is created in the hub corner close to the vane trailing edge, as for the thick vane.

However, the main contribution to the total pressure losses comes from a strongly decelerated flow in the shroud corner near the bump. For all three inlet conditions, one can observe that the flow near the shroud is complex and a pronounced deceleration zone is formed as the bump diffuses the flow. Moreover, this reversal flow is formed in this region, which subsequently downstream develops into a strong vortical structure visible in the downstream vorticity distribution in Fig. 7.

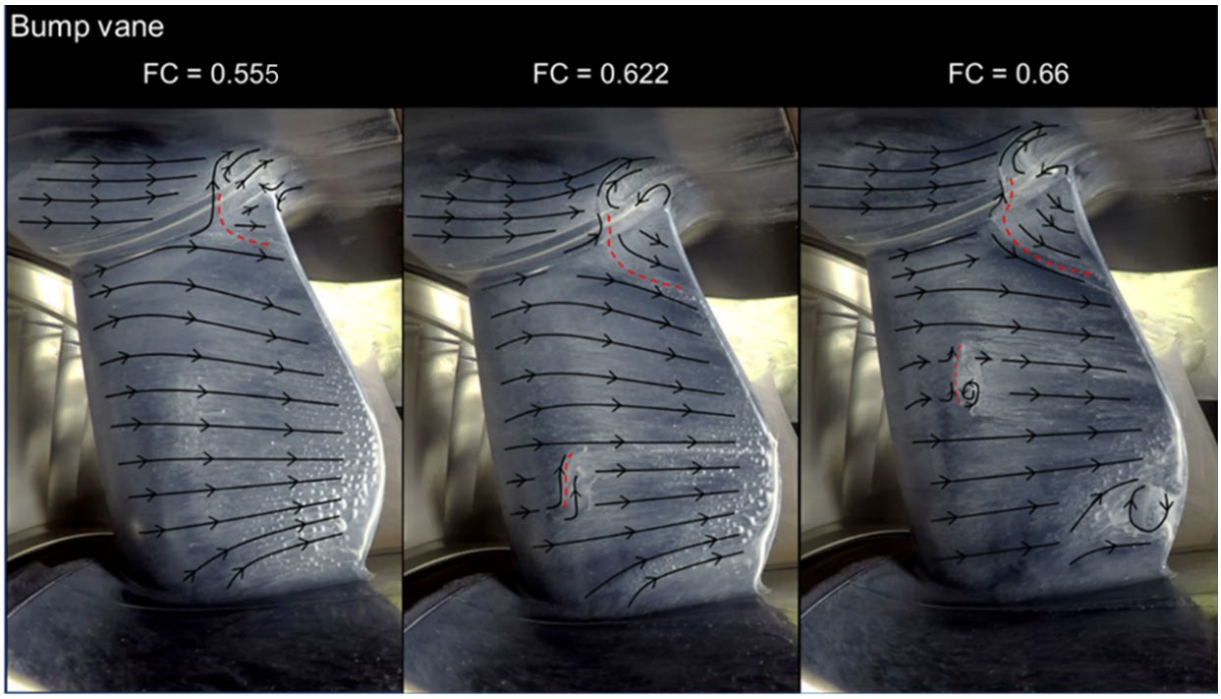

Figure 11: Oil-film visualization for the bump vane at on- and off-design conditions

CONCLUSIONS

In this paper, an engine-realistic TRS configuration with polygonal shroud design and different types of OGVs (regular, thick and bump vane) was experimentally studied for the first time. The experimental measurements, including basic aerodynamic performance and flow visualizations, were carried out at engine-representative flow Reynolds number of 350000 at on- and off-design conditions of the flow swirl angle after the upstream LPT stage.

Based on results from pressure measurements, the thickened vane is shown to have good aerodynamic performance without notable additional losses compared to the regular vane. Flow patterns obtained from the oil-film visualizations indicate two deceleration zones with small separation bubbles and further reattachment, however, does not indicate any reversal flow which proves a good vane design without loss of the turning performance.

Concerning the vane with engine-mount recess, the bump significantly influences the aerodynamics around the OGV. From circumferentially averaged profiles, it was obtained that the bump affects the inlet conditions (swirl angle and total pressure profile) thereby influencing static pressure distribution and vane loading. Blade- and bump-loading analysis shows that bump pressure distribution interacts with vane pressure distribution influenced by the bump itself and, therefore, vane and bump combination should be designed as one aerodynamic unit. The flow around the OGV with a bump is shown to be complex due to the highly diffused boundary layer from the bump. The oil-film visualizations at all three inlet conditions have revealed reversal flow and additional stagnation area in the shroud corner region.

Further downstream, the development of this flow results in an additional vorticity region with twice higher vorticity magnitude compared to the vane wake core. Moreover, for the high loading case, the bump influences the wake intensity in the hub region due to the developed reversal flow, which is confirmed by the results of oil-visualization and wake analysis. As a result, the presence of the bump leads to additional pressure losses for all presented design conditions.

ACKNOWLEDGEMENTS

The authors would like to gratefully acknowledge financial support from the NFFP (Nationella flygtekniska forskningsprogrammet) and the EU-commission. This project has received funding from the Clean Sky 2 Joint Undertaking under the European Union's Horizon 2020 research and innovation programme under grant agreement No 821398. Chalmers Laboratory of Fluids and Thermal Sciences is acknowledged for hosting the facility and for the measurement equipment. The authors would also like to acknowledge the contribution and support by GKN Aerospace Sweden.

REFERENCES

Arroyo, C., (2009). *Aerothermal Investigation of an Intermediate Turbine Duct.* PhD Thesis, Chalmers University of Technology, Gothenburg, Sweden.

Hjärne, J., Chernoray, V., Larsson, J., Löfdahl, L., (2006). *An Experimental Investigation of Secondary Flows and Loss Development Downstream of a Highly Loaded Low Pressure Turbine Outlet Guide Vane Cascade.* Proceedings of ASME Turbo Expo 2006, Paper GT2006-90561.

Hjärne, J., Chernoray, V., Larsson, J., Löfdahl, L., (2007). *Numerical Validations of Secondary Flows and Loss Development Downstream of a Highly Loaded Low Pressure Turbine Outlet Guide Vane Cascade.* Proceedings of ASME Turbo Expo 2007, Paper GT2007-27712.

Hjärne, J., Chernoray, V., Larsson, J., (2008). *Experimental Investigations and Numerical Validation of an Outlet Guide Vane with an Engine Mount Recess.* Proceedings of ASME Turbo Expo 2008, Paper GT2008-50168.

Jonsson, I., Chernoray, V., Dhanasegaran, R., (2019). *Infrared Thermography Investigation of Heat Transfer on Outlet Guide Vanes in an Engine Exit Module.* Proceedings of 13th European Turbomachinery Conference on Turbomachinery Fluid Dynamics and Thermodynamics.

Jonsson, I., Deshpande, S., Chernoray, V., Thulin, O., Larsson, J., (2020). *Experimental and Numerical Study of Laminar-Turbulent Transition on a Low-Pressure Turbine Outlet Guide Vane.* Proceedings of ASME Turbo Expo 2020, Paper GT2020-1787.

Rojo, B., Kristmundsson, D., Chernoray, V., Arroyo C., Larsson J., (2015). *Facility for Investigating the Flow in a Low Pressure Turbine Exit Structure.* Proceedings of 11th European Conference on Turbomachinery Fluid Dynamics and Thermodynamics.

Schönleiner, F., Koch, H., Selic, T., Hoeger, M., Marn A., (2014) *Comparison of the Experimental Results Between a 2D EGV Cascade Test and a Rig Test Under Engine Representative Conditions.* Proceedings of the ASME Turbo Expo 2014, Paper GT2014-26915.

Selic, T., Lengani, D., Marn, A., and Heitmeir, F., (2012*). Aerodynamic Effects of an Unshrouded Low Pressure Turbine on a Low Aspect Ratio Exit Guide Vane.* Proceedings of ASME Turbo Expo 2012, Paper No GT2012-68981.

Sonoda T., Schreiber H., Arima T., (2008). *Endwall Performance of Outlet Guide Vane Cascades With Different Blade Loading Distributions.* Proceedings of ASME Turbo Expo 2008, Paper No GT2008-51111.

Vikhorev, V., Chernoray, V., Thulin, O., Deshpande, S., Larsson, J., (2020). *Detailed Experimental Study of the Flow in a Turbine Rear Structure at Engine Realistic Flow Conditions.* Proceedings of ASME Turbo Expo 2020, Paper No GT2020-15734.

Paper 3

Valentin Vikhorev, Pär Nylander, Valery Chernoray, Jonas Larsson, Oskar Thulin. **Experimental and Numerical Flow Analysis of an Engine-Realistic State-of-the-Art Turbine Rear Structure,** Proceedings of ASME Turbo Expo 2021, GT2021-59224.

Proceedings of the ASME 2021
Virtual Conference and Exhibition
June 7-11, 2021

GT2021-59224

EXPERIMENTAL AND NUMERICAL FLOW ANALYSIS OF AN ENGINE-REALISTIC STATE-OF-THE-ART TURBINE REAR STRUCTURE

Valentin Vikhorev[1], Pär Nylander[2], Valery Chernoray[1], Jonas Larsson[2], Oskar Thulin[2]

[1]Chalmers University of Technology, Department of Mechanics and Maritime Sciences
Gothenburg, SE-41296, Sweden
[2]GKN Aerospace Engine Systems, Trollhättan, SE- 46181, Sweden

ABSTRACT

This paper presents experimental and numerical CFD studies of the aerodynamics of a turbine rear structure (TRS). The TRS test geometry is an engine-realistic state-of-the-art design with a polygonal outer case, recessed engine mount bumps, and three different vane types: regular vanes, bump vanes in bump sectors, and thick vanes. Using three different sector types simultaneously was found to be crucial for the inlet boundary conditions. Experiments were performed in a modern rotating test facility with an LPT stage upstream of the TRS. A Reynolds number of 350,000 was used, representative of a TRS in a narrow-body geared turbofan engine. The TRS performance was analyzed both at on- and off-design conditions and a thorough side-by-side comparison of CFD and experiments was performed. Static-pressure-distributions, turning and outlet flow-angles, wakes and losses, and surface-flow visualizations and outlet total pressure contours are presented. The thick vane showed good aerodynamic performance, similar to the regular vane. For the bump vane, the mount bumps were found to generate additional local separations and secondary flows, resulting in extra losses. In the regions with strong secondary flows CFD over-predicts the wakes, whereas the wakes around midspan, where secondary flows have a smaller influence, are predicted well.

Keywords: low-pressure turbine, turbine rear structure, turbine exhaust casing, turbine rear frame, tail bearing housing, TEC, TRF, TBH, polygonal shroud, outlet guide vane, exit guide vane, engine mount recess, bumps, CFD.

NOMENCLATURE

C_{p0}	total pressure coefficient, $(P_t–P_{tref})/(P_{tref}–P_{sref})$
C_p	static pressure coefficient, $(P_s–P_{sref})/(P_{tref}–P_{sref})$
H	channel height at inlet, m
P_s	static pressure, Pa
P_t	total pressure, Pa
Re	Reynolds number, U_xH/ν
V	blade velocity, m/s
U_x	axial flow velocity, m/s
x	streamwise coordinate, m
ν	kinematic viscosity, m^2/s
Zw	Zweifel coefficient
FC	flow coefficient, U_x/V
θ	angular coordinate, deg

ABBREVIATIONS

FC	flow coefficient
LE	leading edge
LPT	low pressure turbine
NGV	nozzle guide vane
OGV	outlet guide vane
PS	pressure side
SS	suction side
TRS	turbine rear structure

1. INTRODUCTION

In a turbofan engine the rear engine mounts are located in the turbine rear structure (TRS). This structure, placed downstream of the low-pressure turbine (LPT), contains the turbine outlet-guide-vanes (OGV) and also holds the aft bearings for the low-pressure axis. Hence, the TRS is both a structural component, with strong structural loads, and an aerodynamic component that de-swirls the flow from the last LPT rotor. In addition, the TRS vanes must provide the necessary lead-through area for oil and scavenge tubes for lubrication of the bearings. Designing a TRS that can handle both the large structural loads and de-swirl the flow with low pressure losses at all important operating points is always a compromise. Recent trends to improve performance and reduce emissions, increased turbine temperatures, geared engines with an increased off-design range for the TRS, and more strict weight and length requirements have made the TRS design a challenge.

A new state-of-the-art engine representative TRS was designed with a polygonal outer case, recessed engine mounts (bumps), and 12 vanes. The configuration consists of six regular vanes, three thick vanes (also called tube vanes) with increased

thickness and three dedicated bump vanes (also called mount vanes) in the bump sectors. The regular vanes are designed solely for structural and aerodynamic functionality. The additional purpose of the thick vanes is to provide the space needed for oil pipes. The purpose of the engine mount recesses (bumps) and the polygonal shroud is to improve the structural properties of the TRS.

The TRS aerodynamics was experimentally investigated in a modern LPT-OGV test facility at the Chalmers University of Technology. This facility has a shrouded rotating LPT stage upstream of the TRS to provide engine realistic boundary conditions. This facility can reach engine representative Reynolds numbers, and by varying the turbine braking power one can investigate off-design conditions. It is a low-speed large-scale facility that runs at incompressible speeds. The flow in a real engine TRS is fully subsonic, inlet and outlet Mach numbers are around 0.5, with a maximum Mach number just below unity. Hence, the compressibility effects in a real TRS are straightforward to predict – there are no shocks and compressibility mainly influences the local density of the gas, which is easy to model numerically with an ideal gas law.

Numerical CFD analysis was performed to investigate the flow in detail and to compare the numerical results with the experiments. Comparisons were made of static-pressure distributions on the vanes and bumps, losses and wakes, turning and separations as well as secondary flows and surface flow visualizations. Tests were done both at the design point and typical off-design conditions. Overall, the numerical CFD predictions agree well with the experimental results. Further details are described below.

Turbine outlet guide vane flows have previously been studied by several researchers at Chalmers University. Hjärne et al. [1-5] made aero measurements of turbine OGVs and engine mount bumps in a linear cascade test rig. Hjärne et al. [6] also undertook extensive numerical CFD validations. To achieve more realistic inlet conditions and an annular engine representative OGV configuration, Rojo et al. [7] built a rotating test-rig, and the same facility is used in the current work. Rojo [8] also made initial measurements in a simplified circular TRS with only one type of vanes. Jonsson et al. extended these measurements to look at secondary flows [9] and heat-transfer [10] in more detail. Deshpande et al. [11] and Jonsson et al. [12] also studied surface roughness and laminar-turbulent transition in this TRS. Vikhorev et al. [13] continued to experimentally investigate both thick vanes and engine mount bumps in this circular TRS. In 2019 the TRS component was replaced with a more engine representative geometry, having a polygonal shroud, three types of vanes (regular, thick and bump) and recessed engine mount bumps. Initial measurements were published by Vikhorev and Chernoray [14]. The present paper expands these results and adds numerical CFD validations.

The ITTM department at TU-Graz has performed several experimental and numerical studies of TRS aerodynamics. For example, Selic et al. [15] studied the effect of tip-leakage on the TRS, Simonassi et al. [16] studied acoustically optimized vanes and Zenz et al. [17] studied TRS-vanes with riblets.

To the authors' knowledge the present work is the first publication of both experimental and numerical results for a state-of-the-art TRS with three different vane types and a 3D polygonal shroud with engine mount bumps.

2. EXPERIMENTAL DETAILS

In a real aero engine at cruise, the TRS has a Reynolds number, based on channel height and axial velocity, ranging from 10^5 to $6 \cdot 10^5$. This entire range can be covered in the test facility at Chalmers University of Technology. Another important inlet parameter for the TRS is the inlet swirl angle and the corresponding flow coefficient, defined as the ratio between the LPT's rotational speed and the axial velocity. This parameter depends on the turbine work and is controlled in Chalmers' facility by adjusting the turbine torque using a hydraulic brake.

The flow in the facility is cooled by an air-water heat exchanger in order to achieve steady temperature and flow conditions in the test section with high repeatability.

The LPT stage has 60 nozzle guide vanes (NGVs) and a shrouded turbine rotor with 72 rotor blades. Both the LPT-stage and the TRS were designed by GKN specifically for this experimental rig. The designs are engine-representative, but not directly related to any real engine parts. A more detailed description of the facility design can be found in Rojo et al. [7].

A modular design of the TRS test section in the facility enables efficient customization including the possibility to modify channel geometry, any individual OGV or the entire set of OGVs. The investigated configuration of TRS was designed with a polygonal outer case, recessed engine mounts, and 12 vanes arranged as shown in Figure 1. As shown schematically, the test section was equipped with six regular vanes, three thick vanes of increased thickness, and three bump vanes, with each bump vane having a recessed shroud bump.

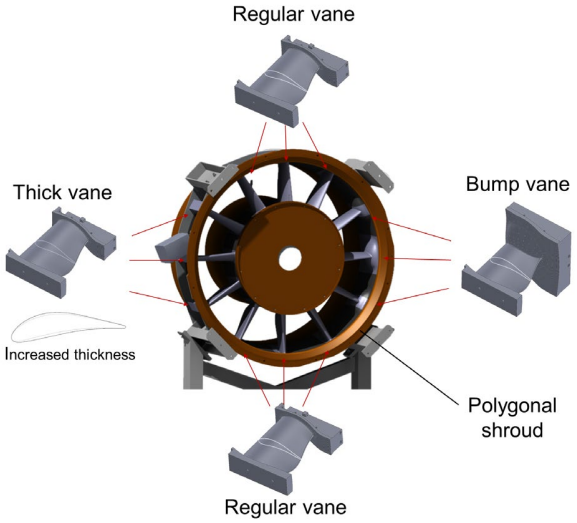

FIGURE 1: Turbine rear structure with implemented outlet guide vanes.

Aero-measurements of the static pressure, total pressure, velocity components and flow angles were made with two multi-hole probes pre-calibrated using in-house calibration protocols. An L-shaped 5-hole probe is located upstream of the OGVs at the inlet plane and turned about 20 degrees respective to the axial direction. A straight 7-hole probe is located downstream of the OGVs at the outlet plane and positioned along the axial direction. Locations of these planes with respect to the OGVs and turbine are shown in Figure 2. The figure also shows the location of the static pressure taps on the OGV.

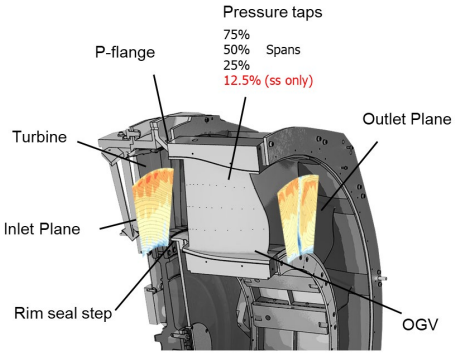

FIGURE 2: Measurement planes and location of the static pressure taps on the OGV.

In order to position the aero-probes, the TRS test section is instrumented with two cylindrical independent traversing systems that are capable of moving in the radial and circumferential directions. Moreover, the downstream probe can be traversed in the axial direction and therefore, the full volume of the TRS can be covered. The accuracy in the positioning of aero probes is 0.01° in a circumferential direction and 0.075 mm in axial and radial directions.

To measure the static pressure distributions a mid-vane of each measurement sector was manufactured with SLA rapid prototyping technology. The vane surface was equipped with 0.7-mm diameter pressure taps located along four spans. Three of the spans (25, 50, and 75%) were used for measurements of pressure distribution over the lower and upper surface of the OGV while a fourth span (12.5%), closest to the hub, was used to obtain static pressure values only on the OGVs suction side. In addition, for the bump vane, the bump was equipped with 96 pressure taps covering the entire bump surface.

A 16-channel digital pressure scanner (PSI-9116, Pressure Systems, Inc.) with a 500-Hz sampling rate was used to acquire pressure values. The sampling time was 2.5 seconds and pressure data was averaged at this time interval. Twelve of the unit's channels were connected to the aero probes while two channels were dedicated to Scanivalve pressure multiplexers for wall static pressure measurements. The remaining two channels were used to obtain reference pressure values from the pitot-static tube located in the bulk region downstream of the OGVs. The static and total pressure data were converted to non-dimensional pressure coefficients (Eq. 1 and 2) using reference pressures.

$$C_{p0} = \frac{P_{\mathrm{t}} - P_{\mathrm{tref}}}{P_{\mathrm{tref}} - P_{\mathrm{sref}}} \quad (1)$$

$$C_{p} = \frac{P_{\mathrm{s}} - P_{\mathrm{sref}}}{P_{\mathrm{tref}} - P_{\mathrm{sref}}} \quad (2)$$

Following a recent study by Jonsson [18] it was chosen to measure the relative pressure with respect to the total reference pressure taken from the pitot-static tube and normalize the values with the dynamic pressure from the pitot-static tube. This is done in order to increase the accuracy of the measurements. This conversion to the non-dimensional form also helps to remove rig-related flow variations unavoidably present in the raw pressure data. Furthermore, other reference values were used for comparison with CFD. The total and static pressure reference values based on area averaging of inlet total and static pressure values were used and calculated as

$$P_{\mathrm{tref}} = \frac{\sum_i P_{\mathrm{t,i}} A_{\mathrm{i}}}{A} \qquad P_{\mathrm{sref}} = \frac{\sum_i P_{\mathrm{s,i}} A_{\mathrm{i}}}{A} \quad (2)$$

where A_{i} is the cell area around the i-th node, A is the inlet plane area, and $P_{\mathrm{t,i}}, P_{\mathrm{s,i}}$ are total and static pressure values for the i-th node.

The visualizations were performed by the oil-film method which is a state-of-the-art tool for obtaining a qualitative survey of the near-surface flow. Based on previous experience, a mixture of oil and TiO_2 powder, with particles from 0.2 to 0.3 μm was selected. The flow patterns were captured by a digital camera whereafter surface streamlines were manually added to the images after dynamic analysis of the flow visualization sequences.

Regarding operating conditions, the experiments were carried out at three different flow coefficients, from 0.555 to 0.66. This corresponds to an average inlet swirl angle between -6.3 and -22.4 degrees, thus spanning a range of 16.1 degrees. The on-design flow coefficient corresponds to the typical cruise flight conditions, the low-loading flow coefficient (low absolute swirl angle) corresponds to sea-level takeoff conditions and the high-loading flow coefficient (high absolute swirl angle) corresponds to a climb point, all points where performance is important. With the Reynolds number set to $3.5 \cdot 10^5$ the inlet flow characteristics are representative of a TRS in a narrow body geared turbofan engine. The TRS operating conditions including the on-design point are summarized and presented in Table 1.

	Operating conditions		
	Low loading / Low swirl (Sea-level takeoff)	On-design (Cruise)	High loading / High swirl (Climb point)
Inlet swirl angle	-6.3	-16.9	-22.4
Flow coefficient	0.555	0.622	0.66
Reynolds number	350,000		

Table 1: Operating conditions.

3. NUMERICAL SETUP

The numerical simulations are done using the commercial CFD solver Fluent 2019R3 by ANSYS. The regular, thick and bump vane are simulated one at a time in a sectorized, single vane model. The computational domain of each sector is meshed by hexahedral elements in the commercial mesh tool ICEM 2019R1. The near wall grid is resolved to achieve $y+$ values below unity in all cases. The computational domains consist of an average of 2.3 M cells, and the final mesh resolution is based on the results from previous mesh sensitivity study. Rotational periodic interfaces are applied on the circumferential boundaries. The circumferential extent of the computational domain in each sector is 30 degree. The computational domain with the mesh resolution on the wall boundaries of the regular vane sector is shown in Figure 3.

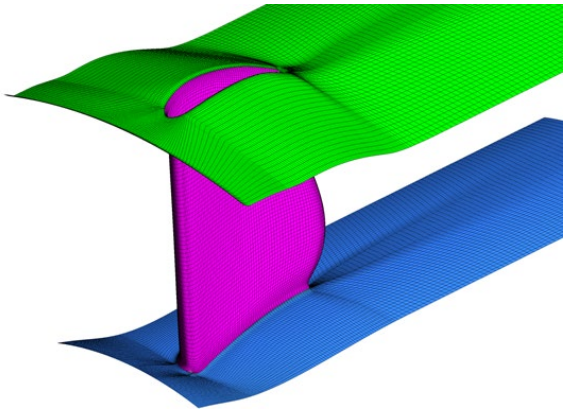

FIGURE 3: The computational domain of the regular sector with wall resolution on hub, vane and shroud.

Steady state RANS simulations are done using the four-equation transition-SST turbulence model by Langtry-Menter [19], also known as the gamma Re-theta ($\gamma-Re_\theta$) model. This turbulence model solves for the $k-\omega$ transport equations and adds two other transport equations, one for the intermittency (γ) and one for the transition onset criteria in terms of the momentum thickness Reynolds number (Re_θ). The model constants in the turbulent transport equations are kept at default in the simulations.

Total pressure and flow angle measurements from the 5-hole probe on the inlet plane (Fig. 2) are used to compute the inlet boundary conditions for the numerical analyses in each sector at each flow condition. The measurement data are used to compute circumferentially averaged radial profiles of total pressure and flow angle components. The radial profiles are applied at the inlet of the computational domain. Inlet turbulence conditions are kept the same and constant in all simulations. The turbulent intensity is 5%, the turbulent length scale is 1.2mm which correspond to experimental values obtained by Jonsson et al. [9].

An average static pressure is set as outlet boundary condition. A radial equilibrium static pressure boundary is used on the outlet, where the static pressure is adjusted to obtain the same mass flow as measured in the experiments. All walls are treated as adiabatic and with smooth no-slip condition.

Surface streamlines in section 4.3 are generated in CFD-Post 2019R3. Other numerical data is visualized using MathWorks MATLAB.

4. RESULTS AND DISCUSSION

In this section wall static pressure, total pressure, and swirl angle distributions, as well as flow visualizations are presented. The results are used to analyze the flow in the TRS and to validate the CFD simulations. The performance of the TRS is considered from the aerodynamic point of view. The performance of CFD is evaluated for prediction capabilities of the TRS aerodynamic performance and secondary flows.

4.1 Inlet conditions

Inlet measurements of total pressure and flow angles were made for a 30-degree sector located upstream of the OGV. Figure 4 shows typical inlet total pressure contours obtained experimentally, and the corresponding inlet values used in CFD. Circumferentially averaged values were used in CFD which means that the circumferential flow non-uniformities were not modelled in the numerical simulations.

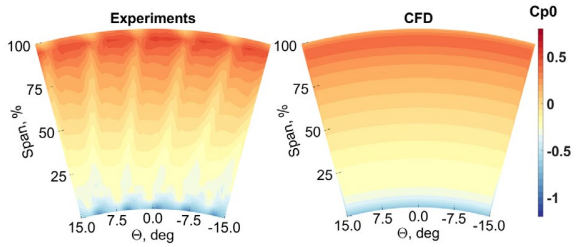

FIGURE 4: Typical inlet total pressure contours (for thick vane at FC=0.555).

The contour plot from the experiment clearly shows five stator wakes coming from upstream NGVs. The wakes are evidenced by the reduced total pressure coefficient. Moreover, counter-rotating vortex pairs coming from each NGV in the hub and shroud regions are clearly visible. The total pressure increases from hub to shroud as expected (Fig. 5 and Ref. [13]) and the absolute value of the inlet swirl decreases (Fig. 5). Experimental profiles are obtained at all operating conditions (see table 1).

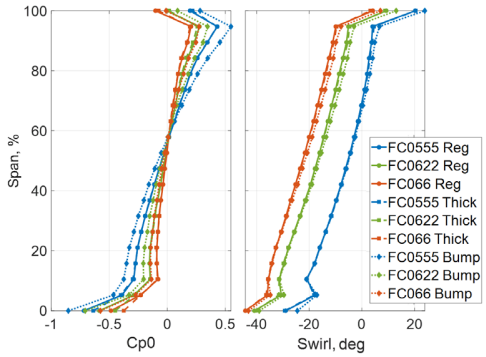

FIGURE 5: Circumferentially averaged inlet total pressure coefficient (left) and swirl angle (right) for the regular, thick and bump vanes at on- and off-design flow coefficients.

The largest inlet swirl magnitude is near the hub, decreasing towards zero near the shroud and attaining opposite swirl direction in the leakage flow region near the shroud. The swirl magnitude increases with the flow coefficient. Notably that the bump vane is showing clear upstream influence on the swirl distributions near the hub and shroud. Furthermore, the bump vane has a pronounced upstream influence on the entire inlet total pressure profile. The thick vane has some visible upstream effect on total pressure near the hub wall and not influencing the inlet swirl. For all cases the radial gradient of the total pressure is decreasing with increased flow coefficient as shown earlier [13, 14]. The inlet profiles illustrate as well that the flow near the shroud is affected by the leakage via the turbine seal and by the presence of the upstream P-flange pocket, shown in Figure 2. The flow near the hub is disturbed by the rim seal step positioned between the stationary and rotating parts.

4.2 Vane static pressure distributions

This section presents vane static pressure distributions, comparing CFD simulations and experiments at 50% span. Measurements are made on all vane types, at the on-design inlet swirl condition (FC=0.622), at the low-swirl off-design condition (FC=0.555) and at the high-swirl off-design condition (FC=0.66).

Figure 6 presents the vane static pressure distributions from the measurements and numerical analyses of all vanes and all flow conditions. Measurement results are shown as symbols and CFD results with solid lines.

The numerical predictions agree very well with the measurements. At the design condition (FC=0.622) all three vane types show similar pressure distributions, with well-placed pressure peaks and no large over-accelerations around the leading edges. As desired, there is a reduced deceleration close to the trailing edges, where the boundary layers are sensitive to flow separation.

At the reduced swirl off-design condition (FC=0.555) all three vane types show a local pressure side over-acceleration around the leading edge. However, the following diffusion is acceptable and no large pressure side separations can be seen. On the suction side the suction peaks are, as expected, reduced and moved aft. Hence, all three vane types show robust aerodynamics and do not show any separation tendencies at the low-swirl off-design condition (FC=0.555).

At the increased swirl condition (FC=0.66) the suction peaks are increased in magnitude and moved forward for all vane types. The pressure distributions are still well-conditioned and there is no local over-acceleration or additional small suction peaks at the leading edges. The loading and the deceleration close to the trailing edges still appears well controlled without any signs of separation. All three vane types show robust behavior also at this high swirl condition.

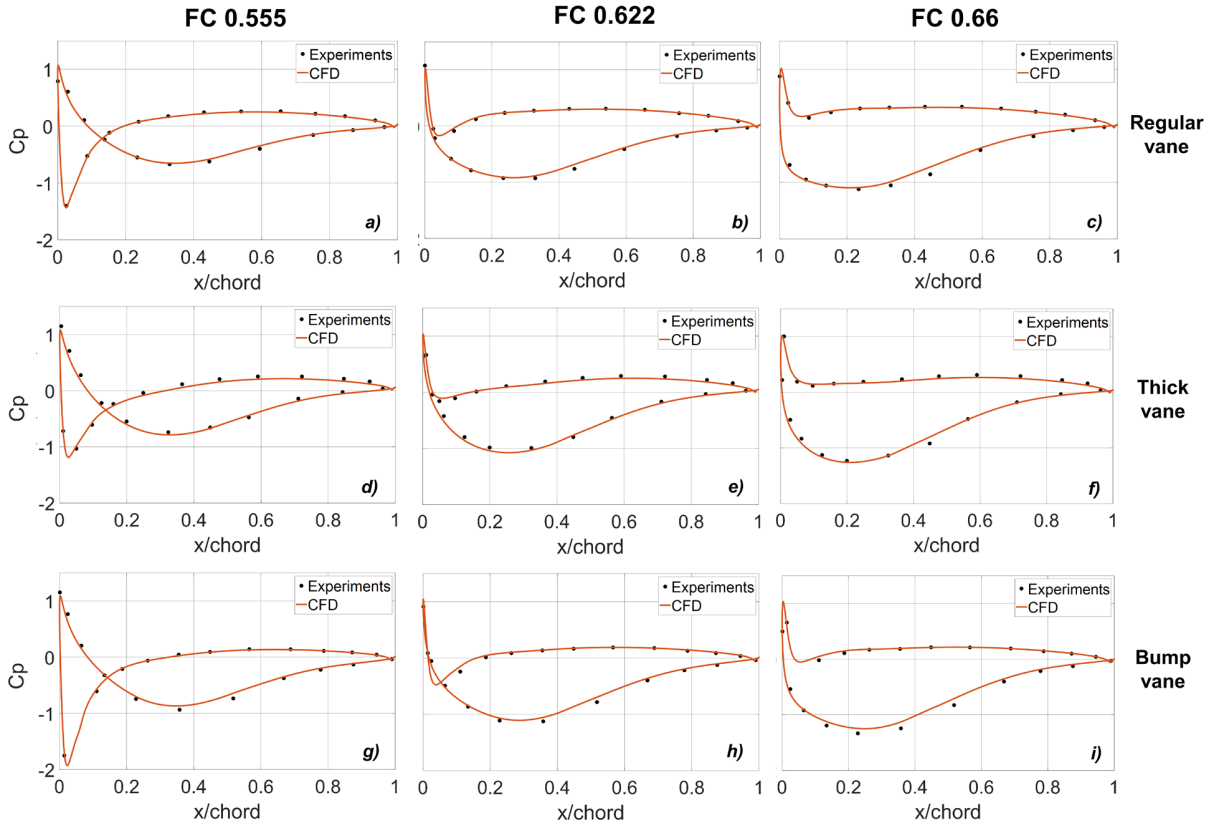

FIGURE 6: CFD predictions and measurements of wall static pressure coefficient distributions at mid-span of the regular, thick, and bump vanes at on- and off-design flow coefficients.

Looking closely at the measurements and comparing them with the numerical results one can see stronger diffusion on the suction sides just downstream of the suction peaks. As was shown in a thorough analysis of Jonsson et al. [12], and supported by the following flow visualizations, at increased inlet swirl, a laminar separation is triggered at midspan on vane suction side at x/c=0.4. This flow separation is not captured by CFD since the CFD is predicting an earlier laminar-turbulent transition. However, since the laminar separation is rapidly reattached after the separation-induced transition, the influence of this separation on the downstream flow is minimal and not affecting the downstream losses in the midspan region.

4.3 Flow visualizations

This section focuses on the analysis of characteristic flow features around OGVs and the influence of flow coefficient and shroud geometry on these features. A comparison between the experimental oil-film visualizations and the CFD predictions of near-wall streamlines is performed. Figures 7-10 present experimental and numerical flow visualizations on the thick and bump vanes at on-design and high loading off-design conditions. These results are shown on the suction side of OGVs since hub suction side corner is found to be the most sensitive to flow separations and plays a significant role in pressure losses [13, 14]. The regular vane case is not shown for the reason that it is very similar to the thick vane case. The low loading case for the suction side is also omitted as it does not reveal any features of particular interest.

Figure 7 shows the flow visualizations for the thick vane at on-design condition. For the experimental case, two small regions with accumulated particles (marked with red solid lines) are clearly visible. The origin of these two regions can be explained by the presence of small local separation bubbles followed by further reattachment. A blue dashed line shows the expected location of laminar-turbulent transition based on the analysis for the previous configuration [11, 12]. Note the position of this line at x/c=0.4 at midspan; camera view angle and optical distortions make the location appear closer to the leading edge than the actual location.

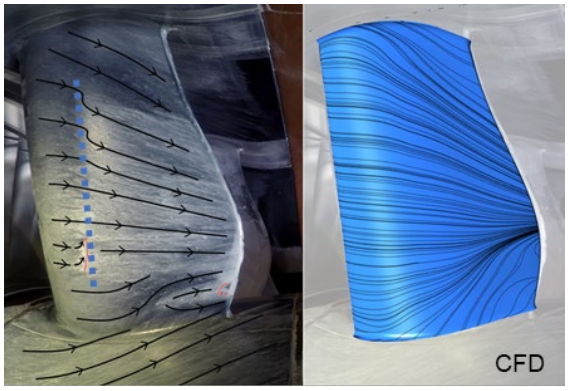

FIGURE 7: Oil-film visualization (left) and near-wall streamlines from CFD (right) on a thick OGV suction side at on-design flow coefficient (FC=0.622).

For the previous configuration [12], a similar separation bubble formed at x/c=0.4 and reattached on the laminar-turbulent transition line at x/c=0.5. The CFD visualization does not indicate the laminar separation bubble at x/c=0.4-0.5 observed in the experiment. Based on the previous findings [12], this is explained by the earlier laminar-turbulent transition in CFD. As a result, the turbulent boundary layer does not separate in CFD. It can be noted, however, that this separation bubble with fast reattachment is not influencing downstream losses as discussed in the previous section. One can observe a typical streamline deviation from hub and shroud towards the 1/3 of vane span in both experiment and CFD. As well, there is a typical streamline distortion near the shroud caused by a mixed effect of the radial pressure gradient and the polygonal shape of the shroud. In the hub corner region, the flow is strongly diffusive and three-dimensional.

For the increased vane loading (Fig. 8), the reverse flow region with accumulated particles near the leading edge is seen to grow and is shifted closer to the shroud, similarly to [13], while the diffusive hub corner region becomes larger and the separated zone in this region becomes larger.

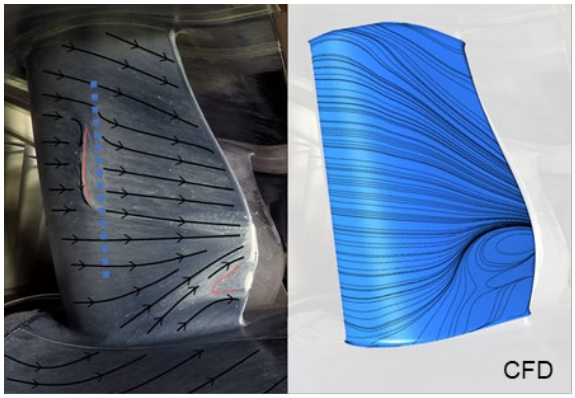

FIGURE 8: Oil-film visualization (left) and near-wall streamlines from CFD (right) on a thick OGV suction side at off-design flow coefficient (FC=0.66).

The CFD simulations capture the increase of the corner region and the increase of the reverse flow zone, however, in CFD the streamlines are more curved, and the reversal zone is larger. Additionally, the CFD result shows more profound flow deflection near the vane trailing edge in the shroud region which can contribute to increased flow diffusion and pressure losses. As can be understood from the comparison of experiment and CFD, in the hub suction side corner close to the trailing edge CFD over-predicts the size of the secondary flow region.

For the bump vane at on-design flow coefficient (Fig. 9), the experimental visualization shows flow separation upstream the transition line very similar to that of the thick vane. The flow in the hub corner region is similar to the thick vane as well. The shroud corner region is strongly affected by the bump and the CFD shows a very similar flow prediction near the vane trailing edge in the bump region. The streamline deflection in this region matches very well with the experiment.

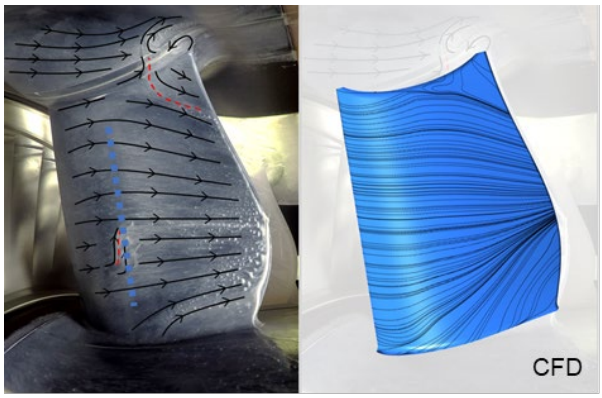

FIGURE 9: Oil-film visualization (left) and near-wall streamlines from CFD (right) on a bump OGV suction side at on-design flow coefficient (FC=0.622).

The visualizations for increased loading case (Fig. 10) demonstrate clear changes in the surface streamlines. The small laminar separation bubble marked with a red dashed line is shifted towards the shroud as with the thick vane. Moreover, a region with reverse flow is created in the hub corner close to the vane trailing edge. CFD shows very good agreement with experimental results except the small laminar separation region upstream of the laminar-turbulent transition line similar to the thick vane case.

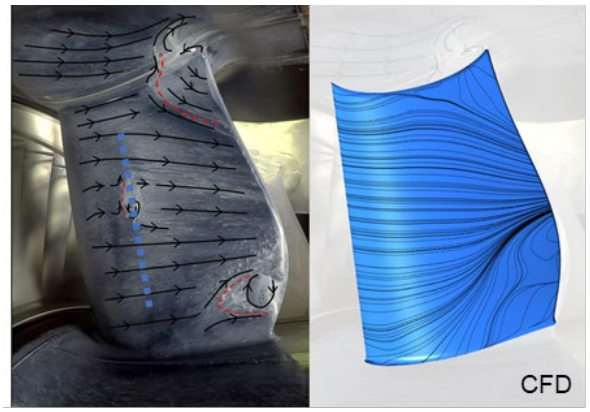

FIGURE 10: Oil-film visualization (left) and near-wall streamlines from CFD (right) on a bump OGV suction side at off-design flow coefficient (FC=0.66).

Figure 11 shows the flow visualizations on the pressure side of bump vane at FC=0.555. It can be noted that there is a quasi-two-dimensional separation bubble formed along the leading edge on the pressure side at FC=0.555 (marked with a red dashed line). The separation bubble extends about 5% chord in the streamwise direction and it is assumed that the flow reattachment occurs due to the laminar-turbulent transition. This separation bubble on the pressure side is not formed at FC=0.622 or 0.66 and well captured with CFD for all vane cases. The flow streamlines on pressure side for other loading cases and other vanes are well predicted by CFD but not shown here.

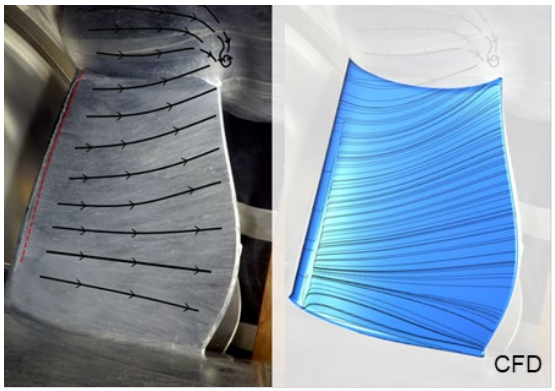

FIGURE 11: Oil-film visualization (left) and near-wall streamlines from CFD (right) on a bump OGV pressure side at off-design flow coefficient (FC=0.555).

4.4 Outlet measurements

In this following section, a comparison is made of the outlet total pressure and swirl angle distributions for all nine cases.

Contours of normalized total pressure for the regular, thick and bump vanes at all three studied flow coefficients are presented in Figure 12. Note that the wake data is shown for about half of the sector, showing the central part containing the OGV wakes. The figure shows a side-by-side comparison of experimental and numerical data. Note the reverse direction of the horizontal axes for agreement with physical set-up in Figure 1. The OGV wakes are shown from downstream the TRS module, while the polar angle increases to positive angles in direction of turbine rotation. In each contour plot the left part of the vane wake corresponds to the pressure side and the right part to the suction side.

For each vane type, one can observe that in experiments the wakes from the vanes are small at the on-design flow coefficient, FC=0.622. In experiments, it can be noted that there is a relatively large region with reduced total pressure at FC=0.555, which is located near the hub on the vane pressure side in all cases. The size of this region is visibly smaller in CFD, which is particularly pronounced for the bump vane case. It can be noted that the losses in this region are predicted rather well in CFD in terms of trends. CFD predicts the largest losses in this region for the bump vane at FC=0.555 and for the other two vanes this part has larger losses at FC=0.555 as compared to other flow coefficients. Both these trends are captured very well by CFD.

Due to the inlet swirl-angle radial gradient, (Fig. 5), the OGV load is larger in the lower spans close to the hub. This increases diffusion and secondary flows in the hub region. The hub boundary layer migrates toward the suction side and rolls up on the vane. A similar, although smaller, secondary flow loss region is formed near the shroud (Fig. 7-10).

Figure 12 shows these secondary flow loss regions close to the end-walls in the suction side areas of the vane wakes. The secondary flows and the corresponding loss regions increase with increased absolute inlet swirl angle, i.e. larger flow coefficient, as expected. In CFD this can be seen as a gradual increase of these loss-regions as the absolute swirl angle and flow coefficient increases.

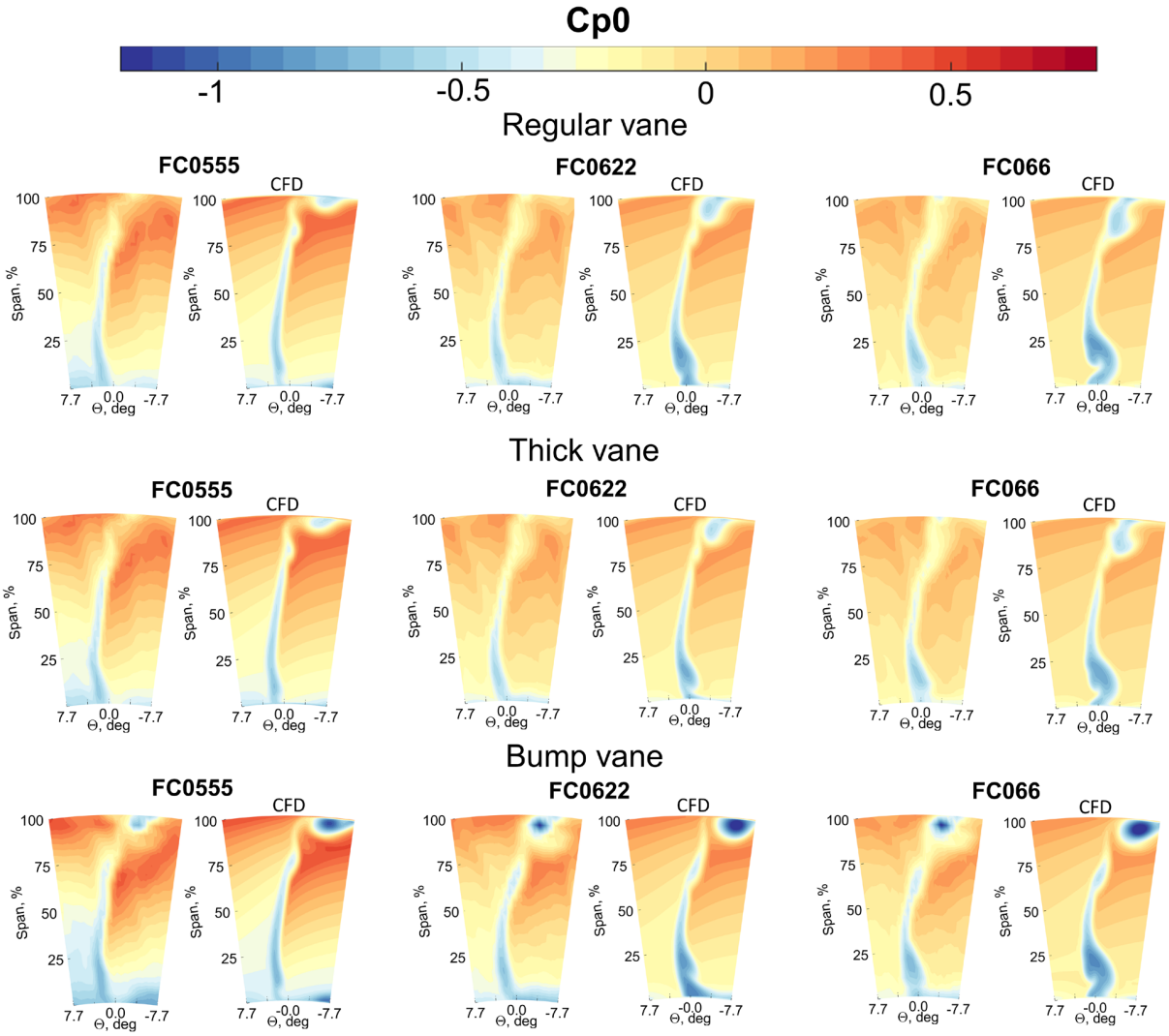

FIGURE 12: Total pressure coefficient distributions at Outlet plane for regular, thick, and bump vanes at on- and off-design flow coefficients. In each contour plot: PS – to the left, SS – to the right.

In experiments, however, there is no obvious change from FC=0.555 to FC=0.622, while there is a clear wake increase from FC=0.622 to FC=0.66. CFD over-predicts the secondary flows and the creation of the associated loss regions in the hub and shroud suction side corners. Overall, CFD predictions are conservative, which is favorable for a reliable design.

From the experimental flow visualization shown for the bump vane (Figs. 9-10) it is evident that apart from the notable flow redistribution, the boundary layers developed in the shroud region near the bump have separated both on the vane, and on the bump itself. Hence, a strong vortical flow region with decelerated fluid is created. The analysis of the streamwise vorticity distributions in the wake, which is not provided here, though the experimental data was included in Ref. [14], shows that the vorticity magnitude in the core of this vortex is about twice as large as in the vane wake region. Therefore, this region with strong vorticity contributes to additional pressure losses which are not present for the regular and thick vanes. The CFD simulations predicts the increase of the pressure loss occurring in the bump-region near the shroud with increased flow coefficient well, although the magnitude is over-predicted in CFD similar to the other vane cases. For the current bump vane design, the bump itself shows acceptable aerodynamic performance. The current configuration has a dedicated mount vane which results in an improved aerodynamic design of the vane-bump combination compared to the previous configuration [13]. The less optimized vane-bump design combination in the previous configuration resulted in additional substantial losses induced in the hub region which is not observed in the current design.

Figure 13 presents detailed comparisons of total pressure wakes at different spans and flow coefficients for the thick vane.

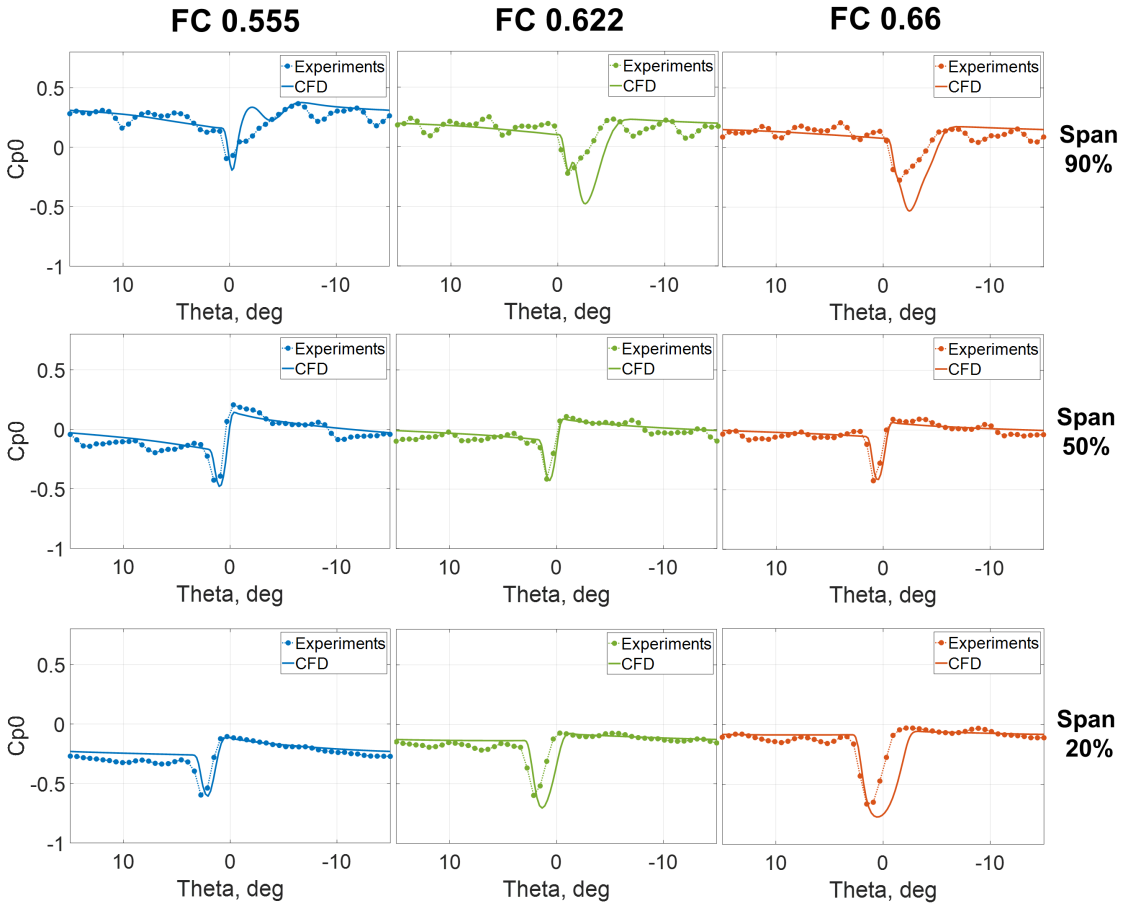

FIGURE 13: Total pressure coefficient distributions for 90, 50, and 20% spans for the thick vane at on-design and off-design flow coefficients.

Wake profiles are presented for a full angular range from 15 to -15 degrees. As clearly seen, the wakes at midspan are predicted very well for all flow coefficients. In the midspan region, secondary flows are less important, and the simulations here predict losses and wake width very well. The wake widths and losses near the hub and shroud are about twice as large in CFD at FC=0.622 and 0.66. This is caused by the previously described over-prediction of secondary flows in these cases.

For the reduced load case (FC=0.555) there is some under-prediction of the wake near the shroud and some under-prediction outside of the wake on the PS-side region with $\theta = 2 - 15$ degrees. The relative change of the wakes with the flow coefficient can clearly be evaluated. The flow becomes more diffusive in the hub region for increased flow coefficient, and this translates to the enlargement of the wake width, as discussed above.

Figure 14 presents comparisons of circumferentially averaged downstream total pressure coefficient for the same cases as in Figure 12. It can be noticed, that the averaged CFD profiles are generally in good agreement with experiments. However, in the regions with intensive secondary flows close to the end-walls, the CFD predictions show some differences from the experiments. In the shroud region, at 70 – 100% span, some differences can be observed for all nine cases. This is the region where the polygonal shroud and circular-polygonal transition regions are located. For the regular and thick vanes at flow coefficient 0.555, CFD under-predicts the losses near the shroud at 85 – 95 % span and over-predicts in close proximity to the shroud. The explanation for this can be seen in the total pressure contours, (Fig. 12), where CFD results over-predict the secondary flow structures. The differences are larger for the bump vane case at FC=0.555 and overall over-prediction can be observed. In the hub region, there is also a typical over-prediction of the variations related to the secondary flow structures for all nine cases. For all three vane geometries, the shape of the total-pressure profiles is very similar and the difference between the CFD and experiments in the strong secondary flow regions near the hub and shroud are relatively small at the on-design flow coefficient, FC=0.622. The total pressure profiles in the region away from the end-walls show the smallest difference between measurements and CFD predictions.

The goal of the aero designer is to design a TRS that de-swirls the flow from the LPT by introducing minimal additional pressure losses, thus obeying two key design criteria.

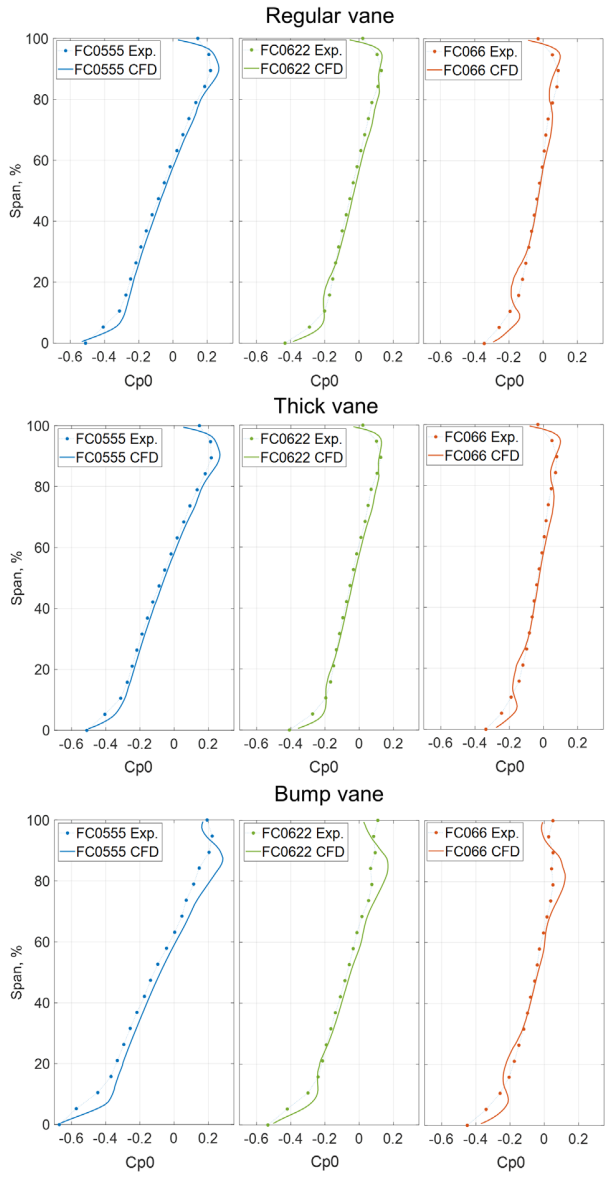

FIGURE 14: Circumferentially averaged total pressure coefficient for the regular, thick and bump vanes at on- and off-design flow coefficients.

The performance of the current OGVs regarding de-swirling the flow from the LPT to axial flow is illustrated in Fig. 15. The figure shows the circumferentially averaged downstream profiles of outlet swirl angle for all studied cases. The aim of a good design is to have the outlet swirl angles close to zero. For the regular and thick vane, the following trends can be seen. In the vicinity to the end-walls, CFD predicts the flow turning well. In the bulk flow at 40–80% span CFD predicts over-turning of the flow with approximately 1 degree relative to the experiments. At 10% span CFD predicts under-turning of the flow with approximately 1 degree in reference to the experiments. The explanation to this is over-prediction of secondary flow structures in the CFD simulations as discussed before. For the bump vane, the flow angle profiles demonstrate a very characteristic swirl change in the shroud region. CFD simulation predicts very well the location of the swirl change and the flow turning in this region, which is a very encouraging result. The best overall prediction is observed for the bump vane at FC=0.555 and for all other cases the prediction of turning is very satisfactory. It is particularly notable that the outlet swirl is closest to zero at on-design flow coefficient (FC=0.622), as intended. The CFD predictions follow the profile variation with varied flow-coefficient well, where the residual swirl increases with increased flow-coefficient. A good prediction of the flow turning angle from the TRS is very important since an incorrect flow turning will result in additional losses due to the residual swirl present in the aero-engine wake.

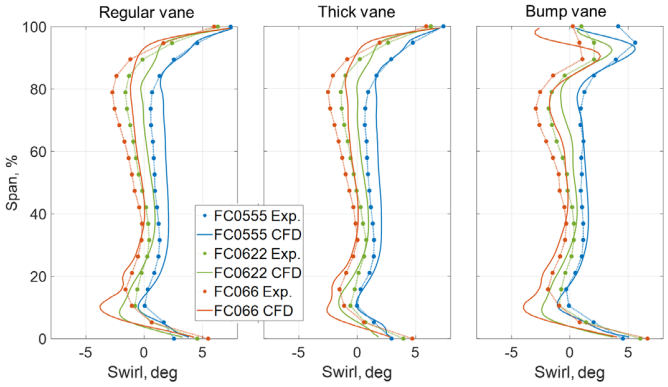

FIGURE 15: Circumferentially averaged outlet swirl angle for the regular, thick and bump vanes at on- and off-design flow coefficients.

Figure 16 shows experimental and numerical incompressible Zweifel coefficients for all studied cases. The definition of incompressible Zweifel coefficient can be found in Coull et al. [20].

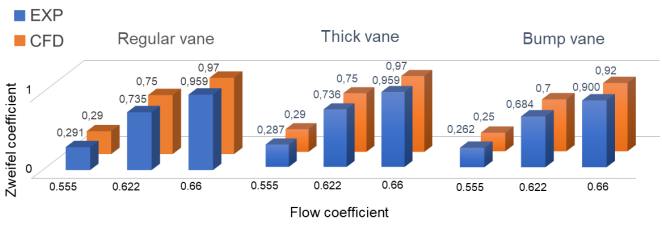

FIGURE 16: Experimental and numerical Zweifel coefficients for the regular, thick and bump vanes at on- and off-design flow coefficients.

As clearly seen, Zweifel coefficient increases with increased flow coefficient. Regular and thick vanes show similar loading which can be explained that overall aerodynamic performance between two vanes is similar. For the bump vane, Zweifel coefficient is lower due to the presence of shroud bump and, hence, reduced inlet swirl angle. However, on-design Zweifel

coefficients are optimal and meet general design requirements (Zw ~ 0.7–0.8). It can be noted, that CFD predicts the Zweifel coefficient well with accuracy better than 0.02 counts for all cases.

5. SUMMARY AND CONCLUSIONS

Aerodynamic measurements and numerical analysis of an engine realistic state-of-the-art TRS with polygonal outer case, recessed engine mount bumps and three different vane types were performed. The study was undertaken in an environment relevant for a geared turbo fan engine at Reynolds number of 350,000 at three different inlet swirl conditions. The numerical results demonstrate good agreement with experiments.

The thick vane shows aerodynamic performance very similar to the regular vane. There is an increase in vane loading with the presence of the mount bump, causing deeper suction peaks on both SS and PS compared to the regular and thick vanes. CFD simulations accurately predict the axial location and depth of suction peaks and diffusion rate aft of the suction peaks on all vanes at all flow conditions.

The comparison of circumferentially averaged radial outlet total pressure profiles shows good agreement outside of the near end-wall regions. CFD predicts larger loss variations in the vicinity of the hub and shroud compared to measurements. The increased loss variations are due to over-prediction of secondary flow structures in CFD. These structures were visualized using the oil-film method in measurements and surface streamlines in CFD and shown to affect the wake width near the hub and shroud regions. CFD over-predicts these wake regions compared to measurements, and the difference increases with increased flow coefficients. Wakes at less loaded flow coefficients, and in the midspan region where the secondary flow structures are less pronounced, are well predicted by CFD.

Moreover, a strong vorticity region evidenced with local pressure drop near the shroud is seen in the bump vane wake. The loss vortex is a consequence of both bump design and acting pressure gradient. This loss vortex is also predicted by CFD, but with somewhat larger extent and magnitude.

From the circumferentially averaged outlet swirl profiles, CFD predictions show good agreement with the measurements. CFD predicts under-turning in highly loaded sections, which is a consequence of the over-prediction of secondary flow structures and hence prediction of earlier flow separation as compared to the measurements. In less loaded regions, where the flow is less prone to separation, CFD predicts overturning of the flow. The measured and predicted loss vortex in the bump sector affects the outlet residual swirl, which is well captured by CFD.

The visualizations at FC=0.622 and 0.66 indicate laminar separation bubbles at *x/c*=0.4-0.5 which is not captured by CFD. According to the previous thorough analysis [12], this is a result of earlier prediction of the laminar-turbulent transition by the $\gamma-Re_\theta$ model. However, since the laminar separation is rapidly reattached after the separation-induced transition, this separation is not affecting the downstream losses in the midspan region. At FC=0.555 there is a quasi-two-dimensional separation bubble formed along the leading edge on the pressure side, which well captured with CFD for all three vane types This separation bubble is not formed at other inlet swirl cases.

The engine realistic TRS with all three vane types mounted simultaneously showed a different upstream influence of different vane types on inlet boundary conditions which is crucial for accurate modelling of TRS aerodynamics.

ACKNOWLEDGEMENTS

The authors would like to gratefully acknowledge financial support from the NFFP (Nationella flygtekniska forskningsprogrammet) and the EU-Commission. This project has received funding from the Clean Sky 2 Joint Undertaking under the European Union's Horizon 2020 Research and Innovation Program under grant agreement No 821398. Chalmers Laboratory of Fluids and Thermal Sciences is acknowledged for hosting the facility and the measurement equipment.

REFERENCES

[1] Hjärne, J., Larsson, J., Löfdahl, L. "Performance and Off-Design Characteristics for Low Pressure Turbine Outlet Guide Vanes: Measurements and Calculations" in *Proc. of ASME Turbo Expo 2006,* Paper GT2006-90550.

[2] Hjärne, J., Larsson, J, Löfdahl, L. "Design of a Modern Test Facility for LPT/OGV Flows" in *Proc. of ASME Turbo Expo 2003,* Paper GT2003-38083.

[3] Hjärne, J., Chernoray, V., Larsson, J, Löfdahl, L. "Experimental Evaluation of the Flow Field in a State-of-the-Art Linear Cascade with Boundary Layer Suction" in *Proc. of ASME Turbo Expo 2005,* Paper GT2005-68399.

[4] Hjärne, J., Chernoray, V., Larsson, J., Löfdahl, L. "An Experimental Investigation of Secondary Flows and Loss Development Downstream of a Highly Loaded Low Pressure Turbine Outlet Guide Vane Cascade" in *Proc. of ASME Turbo Expo 2006,* Paper GT2006-90561.

[5] Hjärne, J., Chernoray, V., Larsson, J. "Experimental Investigations and Numerical Validation of an Outlet Guide Vane with an Engine Mount Recess" in *Proc of ASME Turbo Expo 2008*, Paper GT2008-50168.

[6] Hjärne, J., Chernoray, V., Larsson, J., Löfdahl, L. "Numerical Validations of Secondary Flows and Loss Development Downstream of a Highly Loaded Low Pressure Turbine Outlet Guide Vane Cascade", in *Proc. of ASME Turbo Expo 2007*, Paper GT2007-27712.

[7] Rojo, B., Kristmundsson, D., Chernoray, V., Arroyo C., Larsson J. "Facility for Investigating the Flow in a Low Pressure Turbine Exit Structure" in *Proc of 11th European Conference on Turbomachinery Fluid Dynamics and Thermodynamics*, *ETC 2015*.

[8] Rojo, B., "Aerothermal Experimental Investigation of LPT-OGVs", PhD Thesis, Chalmers University of Technology, Gothenburg, Sweden, 2017.

[9] Jonsson, I, Chernoray, V., Rojo, B., "Surface Roughness Impact on Secondary Flow and Losses in a Turbine Exhaust

Casing" in *Proc. of ASME Turbo Expo 2018*, Paper GT2018-75541.

[10] Jonsson, I., Chernoray, V., Dhanasegaran, R. "Infrared Thermography Investigation of Heat Transfer on Outlet Guide Vanes in an Engine Exit Module" in *Proc. of 13th European Turbomachinery Conference on Turbomachinery Fluid Dynamics and Thermodynamics, ETC 2019*.

[11] Deshpande, S., Jonsson, I., Chernoray, V., "Effect of Surface Roughness on Aerodynamic Performance of Turbine Rear Structure", in *Proc of ASME Turbo Expo 2019*, Paper GT2019-90472.

[12] Jonsson, I., Deshpande, S., Chernoray, V., Thulin, O., Larsson, J., "Experimental and Numerical Study of Laminar-Turbulent Transition on a Low-Pressure Turbine Outlet Guide Vane", in *Proc of ASME Turbo Expo 2020*, Paper GT2020-1787.

[13] Vikhorev, V., Chernoray, V., Thulin, O., Srikanth, D., Larsson, J., "Detailed experimental study of the flow in a turbine rear structure at engine realistic flow conditions", in *Proc of ASME Turbo Expo 2020*, Paper No GT2020-15734.

[14] Vikhorev, V., Chernoray, V., "Experimental Flow Analysis in a Modern Turbine Rear Structure with 3D Polygonal Shroud under Realistic Flow Conditions" in *Proc. of 14th European Turbomachinery Conference on Turbomachinery Fluid Dynamics and Thermodynamics, ETC 2021*.

[15] Selic, T., Lengani, D., Marn, A., and Heitmeir, F. "Aerodynamic Effects of an Unshrouded Low Pressure Turbine on a Low Aspect Ratio Exit Guide Vane", in *Proc of ASME Turbo Expo 2012*, Paper No GT2012-68981.

[16] Simonassi, L., Zenz, M., Zerobin, S, Selic, T., Heitmeir, F. and Marn, A., "On the Influence of an Acoustically Optimized Turbine Exit Casing Onto the Unsteady Flow Field Downstream of a Low Pressure Turbine Rotor", *Journal of Turbomachinery*, 145(4): 041003, 2018.

[17] Zenz, M., Asim, H., Simonassi, L., Leitl, P., Benauer, R., Heitmeir, F. and Marn, A., "Aerodynamical and aeroelastic investigations of a riblet design applied on the surface of turbine exit guide vanes of a low pressure turbine", *Proc. of 14th European Turbomachinery Conference*, *ETC 2019*.

[18] Jonsson, I. "Experimental aerothermal study on internal jet engine structures", Licentiate thesis, Chalmers University of Technology, Gothenburg, Sweden, 2020.

[19] Menter, F. R., R. B. Langtry R.B., Likki S.R., Suzen Y. B., Huang P.G., Völker S. "A Correlation-Based Transition Model Using Local Variables—Part I: Model Formulation". *Journal of Turbomachinery*, 128(3), pp. 413 – 422, 2006.

[20] Coull, J. D., Hodson, H. P. "Blade Loading and Its Application in the Mean-Line Design of Low Pressure Turbines", *Journal of Turbomachinery*, 135(2), 021032, 2013.